

Thalamic dual control of sleep and wakefulness

Thomas C. Gent¹, Mojtaba Bandarabadi¹, Carolina Gutierrez Herrera¹ and Antoine R. Adamantidis^{1,2*}

Slow waves (0.5–4 Hz) predominate in the cortical electroencephalogram during non-rapid eye movement (NREM) sleep in mammals. They reflect the synchronization of large neuronal ensembles alternating between active (UP) and quiescent (Down) states and propagating along the neocortex. The thalamic contribution to cortical UP states and sleep modulation remains unclear. Here we show that spontaneous firing of centromedial thalamus (CMT) neurons in mice is phase-advanced to global cortical UP states and NREM–wake transitions. Tonic optogenetic activation of CMT neurons induces NREM–wake transitions, whereas burst activation mimics UP states in the cingulate cortex and enhances brain-wide synchrony of cortical slow waves during sleep, through a relay in the anterodorsal thalamus. Finally, we demonstrate that CMT and anterodorsal thalamus relay neurons promote sleep recovery. These findings suggest that the tonic and/or burst firing pattern of CMT neurons can modulate brain-wide cortical activity during sleep and provides dual control of sleep–wake states.

Non-rapid eye movement sleep (NREM) is characterized by a predominance of slow waves (0.5–4 Hz) in the neocortex resulting from the synchronized activity of thalamocortical neuronal networks alternating between active (UP) and quiescent (Down) states^{1–3}. During UP states, the membrane potentials of neocortical pyramidal neurons and interneurons are depolarized, which facilitates spiking activity, whereas Down states reflect cell membrane hyperpolarization and neuron spiking quiescence^{1,2,4–6}. Both cortical^{7–10} and thalamic^{11–15} origins have been proposed for the generation of cortical UP states. For instance, isolated cortical circuits spontaneously produce UP and Down states^{7,16}, and a subset of layer V ‘pacemaker’ neurons can recruit larger ensembles of pyramidal neurons to induce UP states *in vitro*¹⁰. On the other hand, pharmacological inactivation of sensory thalamic neurons^{12,13} or cortical deafferentation (i.e., from thalamic, but also brainstem, inputs) inhibits local UP-state initiation in rodents and cats^{2,13,14}. Considering that slow waves in the deafferented cortex have different dynamics (for example, lower frequencies and prolonged Down-state duration) than ones recording from intact brain tissue^{7,8}, together these studies suggest a contribution of the thalamus to the temporal coordination of cortical slow waves during sleep.

Current understanding of the synaptic and cellular mechanisms underlying cortical slow waves stems primarily from investigations into sensory thalamocortical circuits^{1,2,6,16}. However, the cortical heterogeneity^{17,18}, prefrontal cortex origin¹⁹, and brain-wide traveling²⁰ of cortical slow waves suggest the involvement of nonsensory thalamic nuclei, in particular midline and higher-order nuclei. Indeed, excitatory drive from the midline thalamus has emerged as an essential hub for control of cortical excitability^{21,22}, NREM sleep consolidation²³, and consciousness²⁴; however, its precise role in sleep–wake control remains unclear.

We reasoned that midline thalamus neurons may play an important role in pacing cortical UP states during sleep and possibly wakefulness. The mammalian midline thalamus consists of five nuclei that receive extensive input from the brainstem—including from adrenergic, cholinergic, and serotonergic neurons^{25,26}—and from the hypothalamus²⁷, hippocampus²⁸, and prefrontal cortex²⁹. In turn, they project to the cingulate (CING) and insular cortex, as well as to the amygdala, zona incerta (ZI), and striatum^{29,30}.

We therefore investigated the role of midline thalamus neurons in the control of cortical UP states during NREM sleep, sleep–wake behavioral transitions, and sleep recovery using multisite tetrode recordings and optogenetic perturbation in freely behaving mice. We found that burst firing of CMT neurons controlled the onset of CING UP states, while their tonic firing triggered awakening from NREM sleep. Furthermore, we show that brain-wide synchrony of cortical UP states was dependent on a higher-order thalamic relay and promoted sleep recovery. Together, our findings identify a dual role for medial and dorsal thalamic neuron firing in both sleep and wake states.

Results

CMT neurons are phase advanced to the cortical UP state. First, to identify the temporal dynamics of neuron firing from distinct midline thalamic nuclei, we simultaneously recorded the electroencephalogram, electromyogram, local field potentials (LFPs), and unit activity using linear-array electrodes across spontaneous sleep–wake states in freely moving wild-type mice (Fig. 1a,b, Supplementary Fig. 1, and Methods). Notably, we found that CMT neuron activity was significantly phase-advanced to the onset of the UP state underlying the slow wave in CING during NREM (as measured by the half-time of sigmoidal fits of their neuronal spiking activity at the onset of the cortical UP state), as compared to all other neurons from the midline nuclei (CMT versus reuniens, rhomboideus, inter-mediadorsal, and paraventricular nuclei: $P = 0.0073$; $F = 4.422$; degrees of freedom (d.f.) = 4; $n = 22, 23, 7, 28$, and 8 cells, respectively; $n = 6$ animals; one-way ANOVA; Fig. 1c,d and Supplementary Tables 1 and 2).

The non-overlapping connectivity map between the midline and lateral (sensory) thalami suggests distinct functions in cortical control and sleep. To discriminate between these two regions in the control of local UP states in CING and global arousal, we compared neuron spiking activity concurrently in the CMT and ventrobasal complex (VB; CMT: $n = 8$; VB: $n = 8$ cells; $n = 6$ animals) using multisite tetrode recordings (Fig. 2a and see Methods). Both CMT and VB neuron spike rates were strongly modulated across sleep–wake states with high activity during rapid eye movement (REM) sleep (CMT: 25.9 ± 1.6 spikes per s; VB: 35.3 ± 4.1 spikes per s;

¹Centre for Experimental Neurology, Department of Neurology, Inselspital University Hospital Bern, University of Bern, Bern, Switzerland. ²Department of Biomedical Research (DBMR), Inselspital University Hospital Bern, University of Bern, Bern, Switzerland. *e-mail: antoine.adamantidis@dbmr.unibe.ch

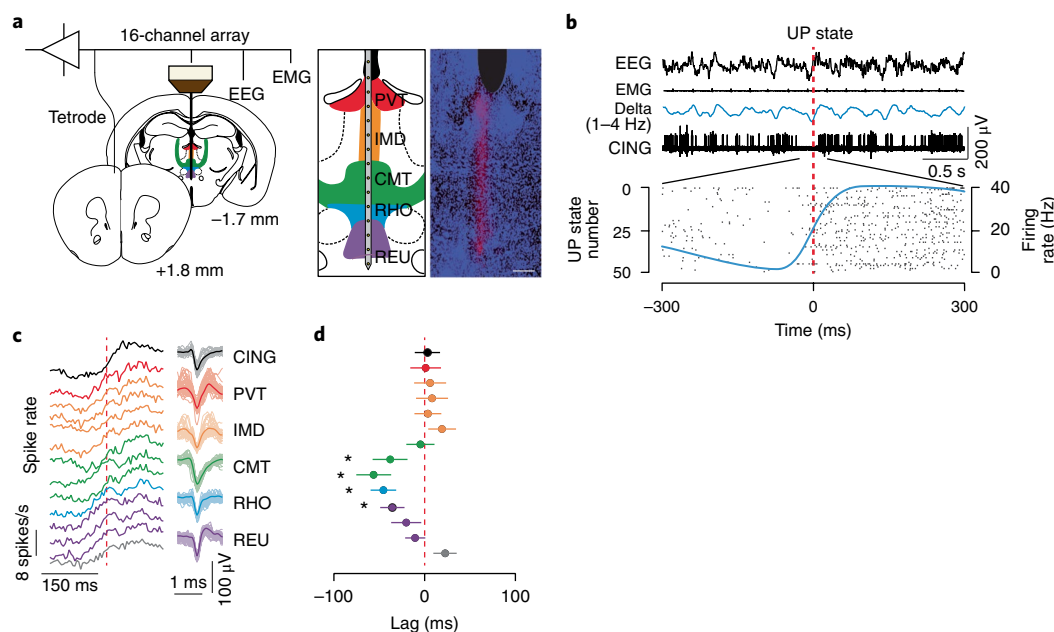


Fig. 1 | CMT neuron spiking is phase-advanced to cortical UP states. **a**, Schematic of instrumentation (left) for chronic recording from 16-channel linear-array electrode in the midline thalamus and tetrode in CING in freely moving mice. Illustration (middle) and anatomical verification (right) of the electrode array placement across the midline thalamic nuclei are shown. Scale bar, 150 μ m. **b**, Representative electroencephalogram (EEG), electromyogram (EMG), LFPs, and neuron unit recordings in CING during NREM sleep. Onset of the cortical UP state is shown by the vertical dashed line (red), which corresponds to the detection of UP states from the EEG based on zero-crossing (see Methods). Raster plot shows spiking activity from a representative CING neuron at the onset of 50 successively detected UP states (bottom) recorded during spontaneous NREM. Average neuronal firing rate for the neuron (based on 10-ms bins) is shown by the blue solid line. Note the sigmoidal shape. **c**, Averaged spiking rate traces for each recording site ($n=13, 8, 8, 6, 6, 8, 7, 7, 8, 8, 8$, and 7 cells from top to bottom, during 28,390 UP states, from $n=6$ animals) at the onset of the UP state (dashed red line) during spontaneous NREM sleep. The gray plot indicates neurons recorded ventral to the midline thalamus. Representative spike waveforms for each nucleus are shown on the right. **d**, Averaged lags \pm s.e.m. of half times from sigmoidal fits of spiking rates at the onset of cortical UP state. Note the CMT neuron spike rate advancement over other thalamic and neocortical neurons. (CMT vs. reuniens (REU), rhomboideus (RHO), inter-mediadorsal nucleus (IMD), and paraventricular nucleus (PVT), $*P=0.0073$; $F=4.422$; d.f. = 4; $n=22, 23, 7, 28$, and 8 cells, respectively, $n=6$ animals; one-way ANOVA;).

$P=0.0087$; $t=4.55$; d.f. = 5; one-sided t test) compared to wake (CMT: 6.3 ± 0.5 spikes per s; VB: 14.7 ± 2.9 spikes per s; $P=0.032$; $t=3.71$; d.f. = 5; one-sided t test) and NREM (CMT: 4.6 ± 1.2 spikes per s; VB: 7.5 ± 0.9 spikes per s; $P=0.041$; $t=3.00$; d.f. = 5; one-sided t test; Fig. 2b and Supplementary Tables 1 and 2). Interspike-interval analysis revealed a predominant bursting pattern of neuron firing in both CMT and VB during NREM (peak interspike interval: wake: CMT: 19.8 ± 6.4 ms; VB: 14.3 ± 5.2 ms; NREM: CMT: 11.1 ± 1.5 ms; VB: 8.9 ± 2.2 ms; REM: CMT: 15.4 ± 3.2 ; VB: 13.6 ± 1.9 ; Fig. 2c,d). However, there was no coherence of spiking activity between CMT and VB cells to UP–Down states (peak interburst interval count: CMT: 173.3 ± 8.3 ms; VB: 65.0 ± 8.9 ms; $P=0.0064$; $t=8.86$; d.f. = 10; two-sided t test; Fig. 2e,f). Notably, spike timing of CMT neurons followed a faithful rhythmicity in advance of the cortical UP state (half-time of sigmoidal curve fits ($t_{1/2}$) = -48.79 ± 12.5 ms, $P<0.01$; $t=4.52$; d.f. = 5; one-sided t test; Fig. 2g) and was also advanced relative to VB neurons ($t_{1/2}$ = $+6.9 \pm 28.4$ ms; $P=0.0008$; $t=9.7$; d.f. = 6; one-sided t test; Fig. 2g,i).

CMT neurons are phase-advanced to behavioral and sleep–wake transitions. Previous investigations of thalamic control of cortical state have focused on primary sensory thalamocortical ‘loops’¹⁶, but others have suggested different roles for midline and sensory thalamus in sleep–wake control³¹, attention, and consciousness^{24,32}. Thus, in the present study, we aimed to compare the cellular activity from thalamic nuclei of different modalities, namely arousal and attention (CMT), sensory (VB), and higher-order thalami across sleep–wake states. In agreement with the phase advancement of CMT

over VB neurons at the onset of cortical UP states, we showed that CMT neuron spiking rates were also advanced over VB neurons during global NREM-to-wake transitions (NREM-to-wake: CMT: -9.2 ± 2.9 ms; VB: 25.9 ± 8.2 ms; $P=0.027$, $t=6.39$; d.f. = 6; wake-to-NREM: CMT: -54.8 ± 14.2 ms; VB: 5.6 ± 6.2 ms; $P=0.0051$, $t=4.16$; d.f. = 6; two-sided t test; Fig. 2h,j and Supplementary Fig. 2). Note that immediately after awakening, CMT and VB neuron spike rates both increased substantially above those seen during wake maintenance and returned to baseline values after ~ 10 s of wakefulness (Fig. 2h). Collectively, these results show that CMT and VB neurons are differentially modulated across sleep–wake states, suggesting distinct functions in controlling cortical excitability.

Activation of CMT but not VB neurons induces rapid wakefulness. Given the phase advancement of the CMT over central and lateral (VB) thalamic neurons during sleep–wake transitions, we tested whether optogenetic activation of CMT neurons induced awakening from natural sleep. To assess this, we targeted the expression of channelrhodopsin (ChR2-EYFP) to excitatory cells in the CMT or VB of wild-type mice using stereotaxic injection of a CaMKII-ChR2-EYFP or CaMKII-EYFP (control) adeno-associated virus 2 (AAV2; Fig. 3a, Supplementary Fig. 3, and see Methods). We then optogenetically activated these areas at a range of frequencies (5–20 Hz; 473 nm) 10 s after the onset of NREM (Fig. 3a,b and Supplementary Figs. 4 and 5 for fidelity responses; see Methods and ref. 3). We found that optogenetic activation of ChR2-EYFP-expressing CMT neurons produced rapid awakening (see Methods) from NREM at all frequencies tested, as compared to control conditions

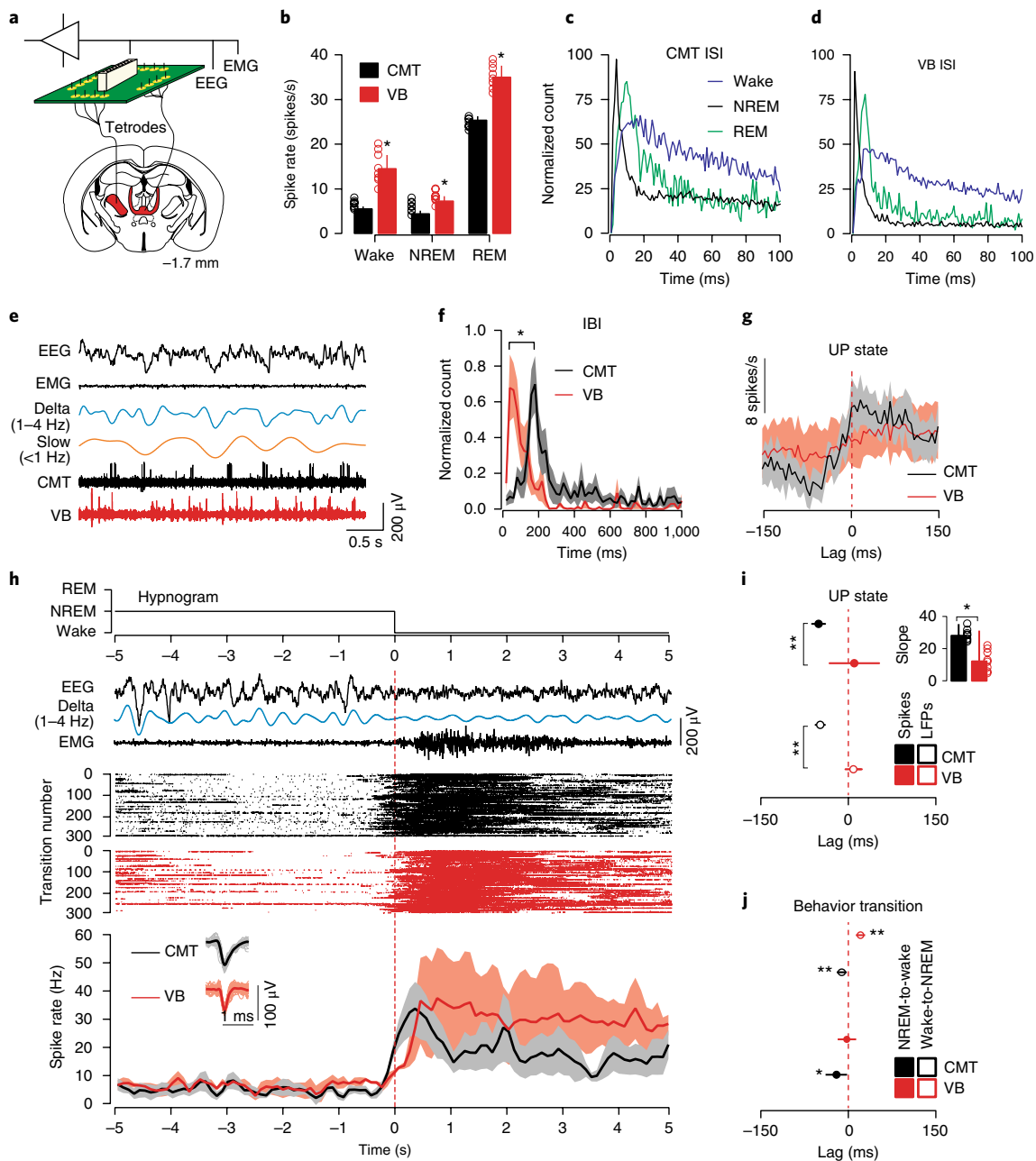


Fig. 2 | CMT neuron spiking is phase-advanced to sensory thalamus and to sleep-wake transitions. **a**, Schematic of instrumentation for chronic simultaneous EEG, EMG, and tetrode recording in CMT and VB in freely moving mice. **b**, Averaged neuron spike rates \pm s.e.m. of CMT (black) and VB (red) neurons across sleep-wake states (wake: $*P=0.032$; $t=3.71$; d.f. = 5; NREM: $*P=0.041$; $t=3.00$; d.f. = 5; REM: $*P=0.0087$; $t=4.55$; d.f. = 5; $n=8$ cells per nucleus from 6 animals; one-sided t test). **c,d**, Averaged interspike intervals (ISI) of CMT (**c**) and VB (**d**) neurons during wake (black), NREM (blue), and REM (green) sleep states. Note the sharp peak due to the bursting activity of thalamic neurons during NREM. **e**, Representative EEG-EMG traces and unit activity of CMT (black) and VB (red) neurons during NREM. Filtered delta (1–4 Hz) and slow oscillations (<1 Hz) are shown. **f**, Interburst intervals (mean \pm s.e.m.) of CMT (black) and VB (red) neurons during NREM. Peaks of interburst interval counts were significantly different for neurons in the two nuclei demonstrating the absence of phase-locking of neuron bursting in the two nuclei. ($*P=0.0064$; $t=8.86$; d.f. = 10; two-sided t test). **g**, Averaged spike rates \pm s.e.m. of CMT (black) and VB (red) neurons at the onset of cortical UP states (dashed red line) during spontaneous NREM. **h**, Representative hypnogram, EEG-EMG, delta (filtered 1–4 Hz), and CMT and VB neuronal spiking activity across NREM-to-wake transitions. Raster plots show spiking activity for one representative cell each in CMT (black) and VB (red) recorded concurrently from the same animal over 300 successive NREM-to-wake transitions during a 6-h electrophysiological recording (Zeitgeber time 3–9). Note that data was scored in 1-s epochs and microarousals were scored as wake events. Averaged neuronal firing rates \pm s.e.m. for CMT ($n=8$ cells; black) and VB ($n=8$ cells; red; from $n=6$ animals) neurons are shown across NREM-to-wake transitions (bottom). Vertical lines (red dashed) indicate the onset of wakefulness. Representative spike waveforms are shown (bottom, inset). **i**, Averaged lags \pm s.e.m. of CMT (black) and VB (red) neuron spike rates (solid) and LFPs (open) at the onset of the cortical UP states (red dashed line). Note the advancement of CMT neuron spiking to cortical UP states compared to VB neuron spiking ($**P=0.0008$; two-sided t test; $t=9.7$; d.f. = 6; one-sided t test). Inset: slope of sigmoidal curve fits for CMT (black) and VB (red) neurons at the onset of the cortical UP state ($*P=0.017$, $t=2.40$; d.f. = 14; two-sided t test). **j**, Averaged lags \pm s.e.m. of CMT (black) and VB (red) neuron spiking rates across NREM-to-wake and wake-to-NREM transitions ($n=8$ cells per nucleus from 6 animals; $*P=0.027$; $t=6.39$; d.f. = 6; two-sided t test).

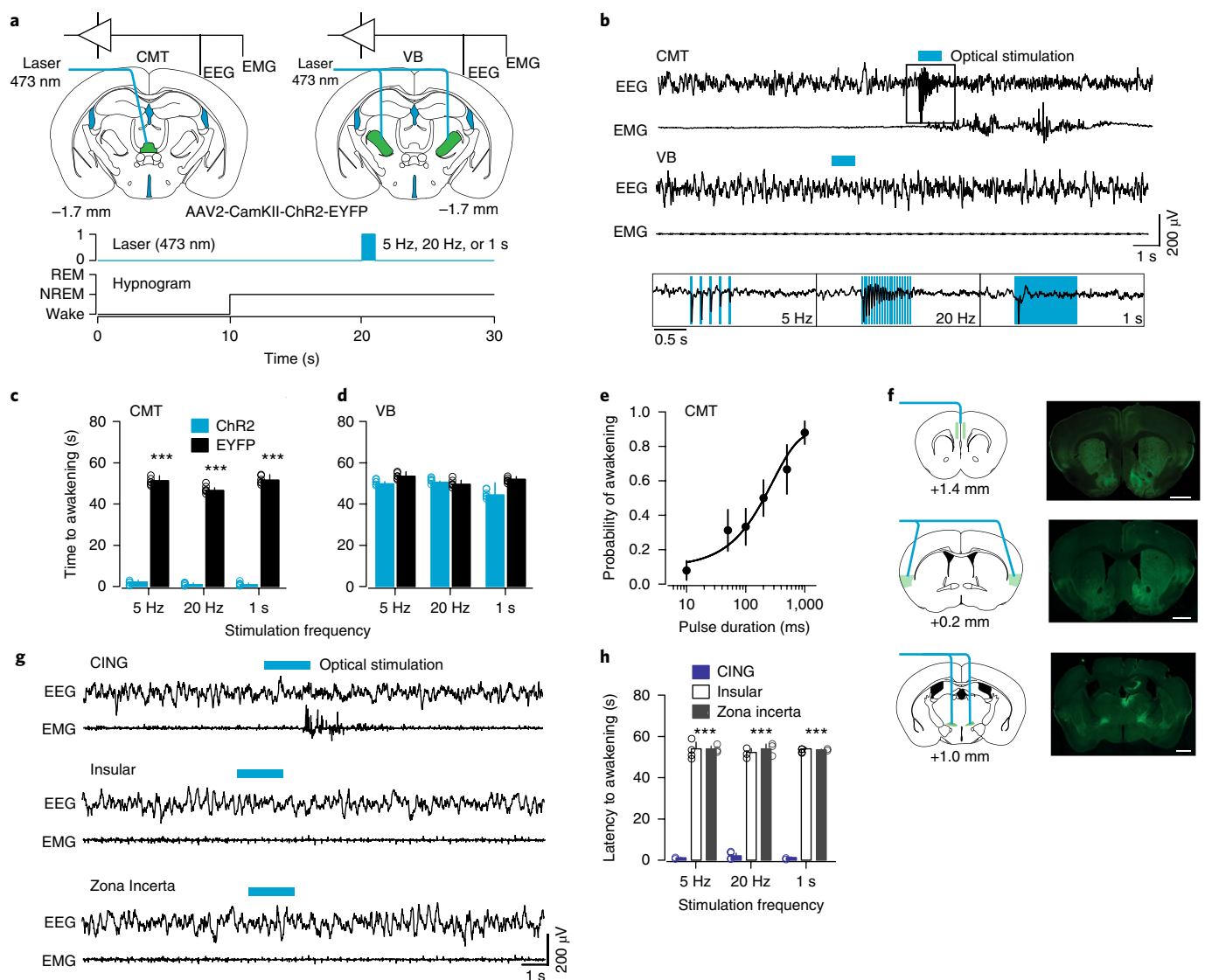


Fig. 3 | Optogenetic activation of CMT, but not VB, neurons entrains cortical UP-like states and induces arousal. **a**, Top: schematic of a brain coronal section illustrating the AAV2-CamKII-ChR2-EYFP or AAV2-CamKII-EYFP (control) injection sites and chronic optical fiber implantation in CMT (left) and VB (right) areas. Bottom: experimental timeline showing blue optical stimulation trains (blue bar) delivered 10 s after the onset of NREM. **b**, Representative EEG-EMG traces from CMT (top) and VB (middle) illustrate arousal responses upon optogenetic activation. Note the high-fidelity entrainment of cortical activity upon optical activation of ChR2-EYFP-expressing CMT neurons at 5 and 20 Hz or continuous illumination (1 s, blue bar; bottom insets). **c,d**, Averaged latencies to awakening \pm s.e.m. following optogenetic CMT (**c**) or VB (**d**) neuron activation ($n=6$ animals per group). Data is based on a minimum of 10 stimulations per frequency per animal (5 Hz: $***P=0.00008$; $t=26.75$; d.f. = 10; 20 Hz: $***P=0.00006$; $t=41.68$; d.f. = 10; 1 s: $***P=0.00006$; $t=27.23$; d.f. = 10; two-sided t test). **e**, Averaged probability of awakenings \pm s.e.m. upon increasing durations of single-pulse optogenetic CMT neuron activation. Values represent Boltzmann sigmoidal curve fit, based on a minimum of 10 stimulations per duration per animal. **f**, Schematic for optogenetic activation of CMT axon terminals (left) and representative photomicrographs of coronal brain sections showing of ChR2-EYFP-expressing CMT axons (right) in CING (top), insular cortex (middle), and ZI (bottom). Scale bar, 1 mm. **g**, Representative EEG-EMG traces illustrate arousal response upon optogenetic activation of ChR2-EYFP-expressing CMT axons in CING (top), insular cortex (middle), and ZI (bottom) at various frequencies (5 Hz, 20 Hz, or continuous, 1 s; blue bar). Note the absence of awakenings upon activation of insular cortex or ZI. **h**, Averaged latencies to awakening \pm s.e.m. upon optical activation of ChR2-EYFP-expressing CMT axon terminals in CING, insular cortex, and ZI (minimum of 10 stimulations per frequency per animal, $n=5$ animals per group). Note that stimulation of CING in nontransfected control animals did not induce awakening ($***P=0.00013$; $F=2567$; d.f. = 2; two-way ANOVA).

(latencies to awakening: 5 Hz: $P=0.00008$; $t=26.75$; d.f. = 10; 20 Hz: $P=0.00006$; $t=41.68$; d.f. = 10; 1 s: $P=0.00006$; $t=27.23$; d.f. = 10; two-sided t test; ChR2: $n=6$ animals; EYFP = 6 animals; Fig. 3b,c and Supplementary Table 3), whereas bilateral optogenetic activations of VB neurons did not (5 Hz: $P=0.23$; $t=2.19$; d.f. = 10; 20 Hz: $P=0.51$; $t=0.63$; d.f. = 10; 1 s: $P=0.46$; $t=1.75$; d.f. = 10; two-sided t test; ChR2: $n=6$ animals; EYFP = 6 animals; Fig. 3b,d).

Single-light-pulse activation of CMT neurons increased the likelihood of NREM–wake transitions in a stimulus-duration-dependent manner (effective dose for 50% awakening (ED_{50}) = 255 ± 23.7 ms; $n=6$ animals; Fig. 3e).

To identify the circuitry involved in CMT neuron-induced awakening, we mapped the CMT efferents using ChR2-assisted mapping by targeting the expression of ChR2-EYFP to excitatory

cells in the CMT neurons of wild type mice stereotactically injected with a CaMKII-ChR2-EYFP AAV2 (Supplementary Fig. 3 and see Methods). Consistent with previous studies²⁹, axonal projections to cortical areas were restricted to CING and insular cortices, while few subcortical terminals were found in the striatum, amygdala, and ZI (Supplementary Fig. 3). No retrogradely labeled cell bodies were found distant from the injection site.

We further showed that optogenetic activation of ChR2-EYFP-expressing CMT axon terminals in CING during NREM recapitulated the rapid awakening seen upon CMT cell-body activation ($P=0.00013$; $F=2567$; d.f.=2; two-way ANOVA; $n=5$ animals; Fig. 3f and see Methods), while no changes were observed upon activation of insular cortex or ZI ($P>0.05$; insular cortex: $n=5$ animals; ZI: $n=5$ animals; Fig. 3g,h and Supplementary Table 3). Light stimulation of CING in nontransfected control animals did not hasten awakening (5 Hz: 54.1 ± 1.6 s, 20 Hz: 55.3 ± 1.7 s; 54.0 ± 1.3 ; CING-control versus insular cortex or ZI: $P>0.05$; one-sided t test; $n=6$ animals; Supplementary Table 3). Notably, layer 5 neurons in CING showed a high-fidelity response to 1-, 5-, and 20-Hz trains of optical stimulation of ChR2-EYFP-expressing CMT neurons (Supplementary Fig. 4). Optogenetic activation of ChR2-EYFP-expressing VB neurons elicited responses only in barrel cortex (BARR) and did not alter CING neuronal activity (Supplementary Fig. 5). These results show that tonic firing duration, rather than frequency, of CMT neuron activity controls NREM-wake transitions, while VB neurons seem to have minimal involvement in sleep-wake state control.

Brain-wide synchronization of CMT neuron-induced UP-like states is dependent on a dorsal thalamic relay. CMT neuron firing was phase-advanced to cortical UP states (Fig. 2). This raises the question of whether CMT neurons actually contribute to the initiation of UP states and, if so, through what neural circuit. Consistent with previous studies^{29,30}, we found no CMT neuron projections in posterior neocortical areas, other areas of the thalamus (except the ZI), or in the brainstem (Supplementary Fig. 3), leaving open the possibility of either corticocortical or cortico-thalamocortical³³ spreading of excitatory signals supporting the propagation of UP states¹⁹. To test for the presence of a thalamic relay, we first mapped CING neuron efferents by targeting the expression of ChR2-mCherry to excitatory cells in the CING (layer 5) of wild-type mice by stereotactic injection of a CaMKII-ChR2-mCherry AAV2 in the same anteroposterior segment in which we had found afferents from CMT neurons (Supplementary Fig. 6 and see Methods).

We found sparse, short-range cortical projections to M1 area and diffuse, low-intensity projections throughout most of the lateral and reticular thalamic nuclei, suggesting that propagation of activity from the CMT-CING network may reach distant cortices via an indirect thalamic route (Supplementary Fig. 6). Indeed, the densest terminals were observed in the anterodorsal nucleus of the thalamus (AD; Supplementary Fig. 6), suggesting a relay function for those cells. Unlike CMT cells, AD neurons have broad cortical projections³⁴ and therefore represent a potential candidate for initiating widespread cortical UP states. Supporting this, we mapped AD efferents by targeting the expression of archaerhodopsin (ArchT-EYFP) to excitatory cells in AD of wild-type mice stereotactically injected with a CaMKII-ArchT-EYFP AAV2 and found extensive ipsilateral projections, possibly via an axonal tract ventral to the laterodorsal thalamus, across most areas of the posterior cortex in both layers 1 and 4, including the visual cortex (VIS), as well as the retrosplenial cortex as shown previously³⁴ (Supplementary Fig. 7).

To demonstrate the relay nature of AD neurons within the CMT-CING-AD-VIS circuit, we used a combinatorial optogenetic approach, targeting expression of ChR2 and ArchT to excitatory CMT and AD neurons using stereotactic injection of CaMKII-ChR2-EYFP and CaMKII-ArchT-EYFP AAV2s,

respectively. Optical fibers were chronically implanted dorsal to the CMT and AD areas, and neuron activity and LFPs were simultaneously recorded from CMT, AD, CING (layer 5), BARR (layer 5), and VIS (layer 5) areas using multisite tetrode recordings in freely moving animals (Fig. 4a,b and see Methods). We recorded neurons in layer 5 as it is the proposed site of cortically generated slow oscillations and the locus of corticofugal projections¹⁰. We first found that CMT, CING, AD, BARR, and VIS spiking rates were all modulated across sleep-wake states (Supplementary Fig. 8 and Supplementary Table 1).

Confirming our initial findings (Fig. 1), phase-locking values—determined from $t_{1/2}$ values indicated that a CMT-CING network may initiate cortical UP states (CMT: $P<0.01$; $t=4.30$; d.f.=7; $n=9$ cells; CING: $P<0.05$; $t=4.08$; d.f.=7; one-sided t test; $n=8$ cells; $n=6$ animals; Supplementary Fig. 8 and Supplementary Table 1), as has been suggested based on recordings in anesthetized rats³¹. We showed that optogenetic burst-like activation of ChR2-EYFP-expressing CMT neurons consistently induced UP-like states in the CING cortex (Fig. 4c,d, Supplementary Fig. 9, and Supplementary Tables 1 and 2). We found no difference between spontaneous or optogenetically induced slow-wave activity, as measured by average duration of UP and Down states in CING (Fig. 4e-g; UP: $P=0.45$; $t=0.87$; d.f.=7; Down: $P=0.56$; $t=0.66$; d.f.=7; two-sided t test; $n=8$ animals). Notably, temporal lags of UP-like states between CMT, CING, AD, and VIS cells suggested a serial, rather than parallel, pathway (CMT-to-CING: $P<0.00009$; $t=9.18$; d.f.=8; CING-to-AD: $P=0.000017$; $t=22.35$; d.f.=8; AD-to-BARR: $P=0.0068$; $t=3.621$; d.f.=8; AD-to-VIS: $P=0.0094$; $t=7.18$; d.f.=8; BARR-to-VIS: $P=0.64$; $t=0.49$; d.f.=8; one-sided t test; Fig. 4h and Supplementary Table 1). To further confirm this finding, we showed that optogenetic silencing of ArchT-EYFP-expressing AD neurons completely prevented the induction of UP-like states in VIS neurons by optogenetic driving of ChR2-EYFP-expressing CMT neurons (Fig. 4d). Consistent with the low coherence between midline and lateral sensory thalamic circuit activity, UP-like states in BARR were minimally affected by CMT neuron activation and AD neuron silencing in this experiment (Fig. 4d and Supplementary Fig. 4). Notably, unilateral optical silencing of AD significantly prolonged the duration of NREM episode duration (spontaneous versus unilateral silencing, $P=0.0014$; spontaneous versus bilateral silencing, $P=0.0025$; one-sided t test; Supplementary Fig. 10).

To determine the contributions of each hub of the CMT-CING-AD-VIS network, we targeted expression of ArchT-EYFP to excitatory neurons of CMT, CING, and AD in separate cohorts of animals, by stereotactic injection of CaMKII-ArchT-EYFP or CaMKII-EYFP AAV2s (control) and optogenetically silencing ArchT-EYFP-expressing neurons during NREM sleep (Fig. 5a,b,j,o). Consistent with our optogenetic activation results, silencing of ArchT-EYFP-expressing CMT neurons decreased synchrony (as measured by the slope of modulation and the onset of cortical UP state) in layer 5 CING and VIS neurons, but not in layer 5 BARR cortex neurons (CING: $P=0.008$; $t=2.66$; d.f.=16; $n=9$ cells; BARR: $P=0.96$; $t=0.05$; d.f.=10; $n=6$ cells; VIS: $P=0.002$; $t=3.87$; d.f.=14; $n=8$ cells; from $n=6$ animals; two-sided t test; Fig. 5c-f). Notably, optogenetic silencing of CMT neurons also reduced phase synchrony between CMT, CING, AD, and VIS in ArchT-EYFP-expressing animals compared to controls (Fig. 5g,h). This was accompanied by a decrease of CING slow-wave power ($P=0.008$; $t=4.809$, d.f.=5; Fig. 5i) that was consistently followed by a rebound in slow-wave power ($P=0.005$; two-sided t test; $t=5.02$; d.f.=5; $n=6$ animals; Fig. 5i).

We further found that optogenetic silencing of CING neurons reduced synchrony in VIS neurons ($P=0.014$; two-sided t test; $t=3.99$, d.f.=4), but not BARR neurons ($P=0.86$; $t=1.02$; d.f.=4; $n=6$ cells; from $n=5$ animals; two-sided t test; Fig. 5j-m), and decreased normalized slow-wave power in VIS ($P=0.036$;

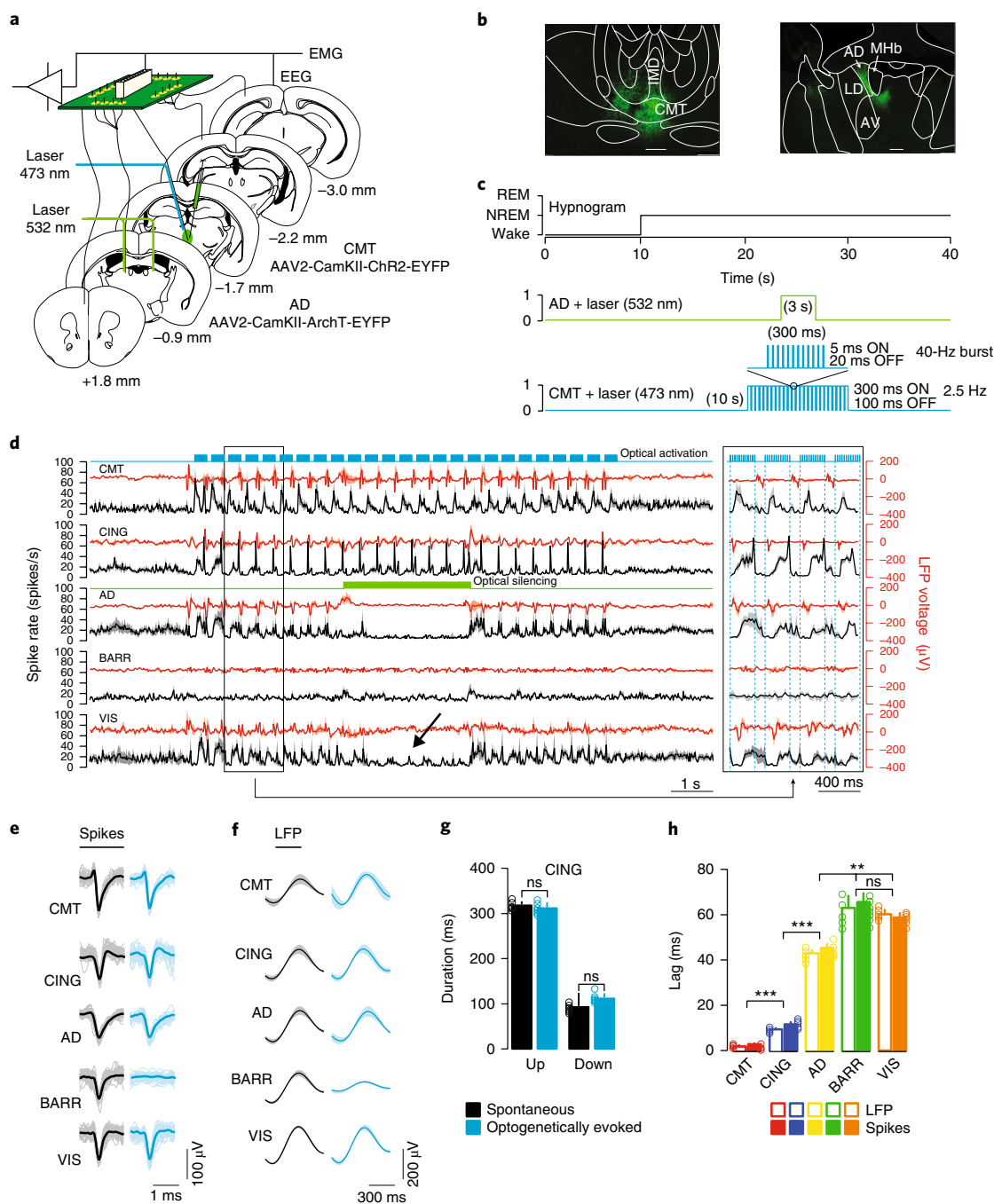


Fig. 4 | AD neurons relay CMT-induced UP-like states to posterior cortical areas. **a**, Schematic of instrumentation for chronic implantation of multisite tetrode recordings from CMT, CING, AD, BARR, and VIS and optic fiber implants over CMT and AD (bilaterally). AAV2-CaMKII-ChR2-EYFP and AAV2-CaMKII-ArchT-EYFP were stereotactically injected into CMT and AD (bilaterally), respectively. **b**, Representative photomicrographs of coronal brain sections showing ChR2-EYFP-expressing CMT neurons (left) and ArchT-EYFP expressing AD neurons (right). Scale bar, 100 μ m. Note the projections from CMT and AD neurons extending to the centrolateral nucleus and internal capsule, respectively. LD, laterodorsal nucleus; AV, anteroventral nucleus; MHb, medial habenular nucleus. Data repeated in $n=6$ animals. **c**, Experimental timeline showing blue optical activation of UP-like states (5-ms pulses, 300 ms ON, 100 ms OFF, 10-s duration) in CMT neurons and green optical silencing (3 s) of AD neurons, delivered 10 s after the onset of NREM. **d**, Averaged traces \pm s.e.m. of CMT ($n=9$ cells), CING ($n=8$ cells), AD ($n=9$ cells), BARR ($n=9$ cells), and VIS ($n=8$ cells; from $n=6$ animals) neuron spiking activity (black) and LFP voltage (red) during combinatorial optogenetic experiments. Note the high fidelity of CMT-induced UP-like states traveling along the CING-AD-VIS pathway and the complete blockade of spike transfer to VIS upon AD silencing (arrow). An expanded view of the traces illustrating the lag of entrainment is shown on the right. **e**, Representative spike waveforms for spontaneous (black) and CMT-evoked (blue) neuronal firing in CMT, CING, AD, BARR, and VIS. **f**, Average waveforms \pm s.e.m. of spontaneous (black) and CMT-evoked (blue) UP states in CMT, CING, AD, BARR, and VIS ($n=8$ animals). **g**, Average durations of spontaneous (black) and evoked (blue) UP and Down states in CING (UP: $P=0.45$; $t=0.87$; d.f. = 7; Down: $P=0.56$; $t=0.66$; d.f. = 7; two-sided t test; $n=8$ animals; ns = not significant). **h**, Averaged neuron spiking and LFP lags \pm s.e.m. from CMT (red), CING (blue), AD (yellow), BARR (green), and VIS (orange) upon optical activation of ChR2-EYFP-expressing CMT neurons. (CMT-to-CING: $***P=0.00009$; $t=9.18$; d.f. = 8; CING-to-AD: $***P=0.00017$; $t=22.35$; d.f. = 8; AD-to-BARR: $**P=0.0068$; $t=3.621$; d.f. = 8; AD-to-VIS: $**P=0.0094$; $t=7.18$; d.f. = 8; BARR-to-VIS: $P=0.64$; $t=0.49$; d.f. = 8; one-sided t test; ns = not significant).

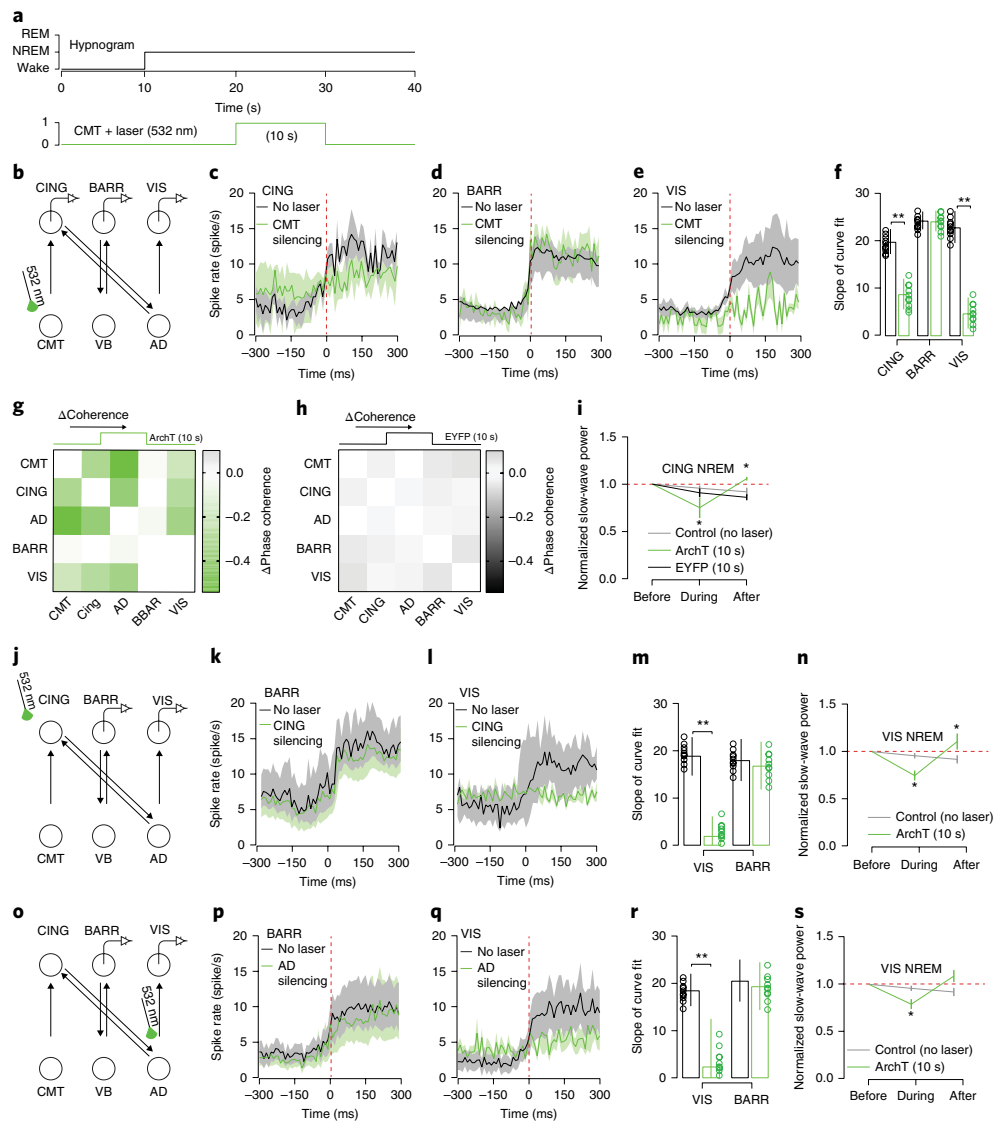


Fig. 5 | CMT neuron firing is necessary for cortical UP-state synchrony. **a**, Experimental timeline showing optical silencing (10 s, 532 nm) of ArchT-expressing CMT neurons 10 s after the onset of NREM. **b**, Schematic of N-type circuit and instrumentation for chronic implantation of multisite tetrode recordings from CING, BARR, and VIS and optic fiber implants over CMT. AAV2-CaMKII-ArchT-EYFP was stereotactically injected into CMT. **c–e**, Average spiking rates \pm s.e.m. for CING (**c**; $n = 9$ cells), BARR (**d**; $n = 6$ cells), and VIS (**e**; $n = 8$ cells; from $n = 6$ animals) neurons at the onset of the cortical UP states (red dashed line). Note that silencing of EYFP-expressing CMT neurons (control) did not significantly change spiking rates in CING ($P = 0.44$; $t = 1.74$; d.f. = 16; $n = 9$ cells; $n = 6$ animals; two-sided t test). **f**, Average slope \pm s.e.m. of curve fits for spiking rates at the start of cortical UP state (CING: $**P = 0.008$; $t = 2.66$; d.f. = 16; $n = 9$ cells; BARR: $P = 0.96$; $t = 0.05$, d.f. = 10; $n = 6$ cells; VIS: $**P = 0.002$; $t = 3.87$; d.f. = 14; $n = 8$ cells; from $n = 6$ animals; two-sided t test). **g, h**, Averaged change in phase coherence for CMT, CING, AD, BARR, and VIS for optical silencing of CMT neurons expressing ArchT-EYFP (**g**) and EYFP (**h**). **i**, Averaged delta power \pm s.e.m. of LFP signals recorded in CING 10 s before, during, and 10 s after optogenetic silencing of ArchT- (green) or EYFP-expressing (black) CMT neurons compared to control conditions (gray). Delta power is normalized to the first 10 s of NREM. Note the rebound in delta activity after CMT neuron silencing (dotted red line; $*P = 0.005$; two-sided t test; $t = 5.02$; d.f. = 5; $n = 6$ animals compared to normalized value of 1). **j**, Schematic of N-type circuit and instrumentation for chronic implantation of multisite tetrode recordings from BARR and VIS and optic fiber implants over CING. AAV2-CaMKII-ArchT-EYFP was stereotactically injected into CING. **k, l**, Average spiking rates \pm s.e.m. for BARR (**k**; $n = 6$ cells) and VIS (**l**; $n = 6$ cells; from $n = 5$ animals) neurons at the onset of the cortical UP states (red dashed line). **m**, Average slope \pm s.e.m. of curve fits for spiking rates at the onset of cortical UP states. (BARR: $P = 0.86$; $t = 1.02$; VIS: $**P = 0.014$; $t = 3.99$; d.f. = 4; two-sided t test). **n**, Averaged delta power \pm s.e.m. in VIS 10 s before, during, and 10 s after optogenetic silencing of ArchT-expressing CING neurons (green; $*P = 0.036$; one-sided t test; $t = 3.99$; d.f. = 3; one-sided t test; from $n = 5$ animals) and control conditions (gray). Delta power is normalized to the first 10 s of NREM. Note the rebound in delta activity after CMT neuron silencing (dotted red line; $*P = 0.039$; one-sided t test; $t = 3.45$; d.f. = 3; one-sided t test; compared to normalized value of 1). **o**, Schematic of N-type circuit and instrumentation for chronic implantation of multisite tetrode recordings from BARR and VIS and optic fiber implants over AD. AAV2-CaMKII-ArchT-EYFP was stereotactically injected into AD. **p, q**, Average spiking rates \pm s.e.m. for BARR (**p**; $n = 9$ cells) and VIS (**q**; $n = 10$ cells; from $n = 6$ animals) neurons at the onset of the cortical UP states (red dashed line). **r**, Average slope \pm s.e.m. of curve fits for spiking rates at the start of the cortical UP state (BARR: $P = 0.75$; $t = 1.73$; d.f. = 7; $n = 9$ cells; VIS: $**P = 0.036$; $t = 6.84$, d.f. = 8; $n = 10$ cells; $n = 6$ animals; two-sided t test). **s**, Averaged delta power \pm s.e.m. in VIS 10 s before, during, and 10 s after optogenetic silencing of ArchT-expressing AD neurons (green) and control conditions (gray). Delta power is normalized to the first 10 s of NREM. Note the rebound in delta activity after CMT neuron silencing (dotted red line; $*P = 0.011$; $t = 4.63$; d.f. = 4; from $n = 6$ animals; one-sided t test; compared to normalized value of 1).

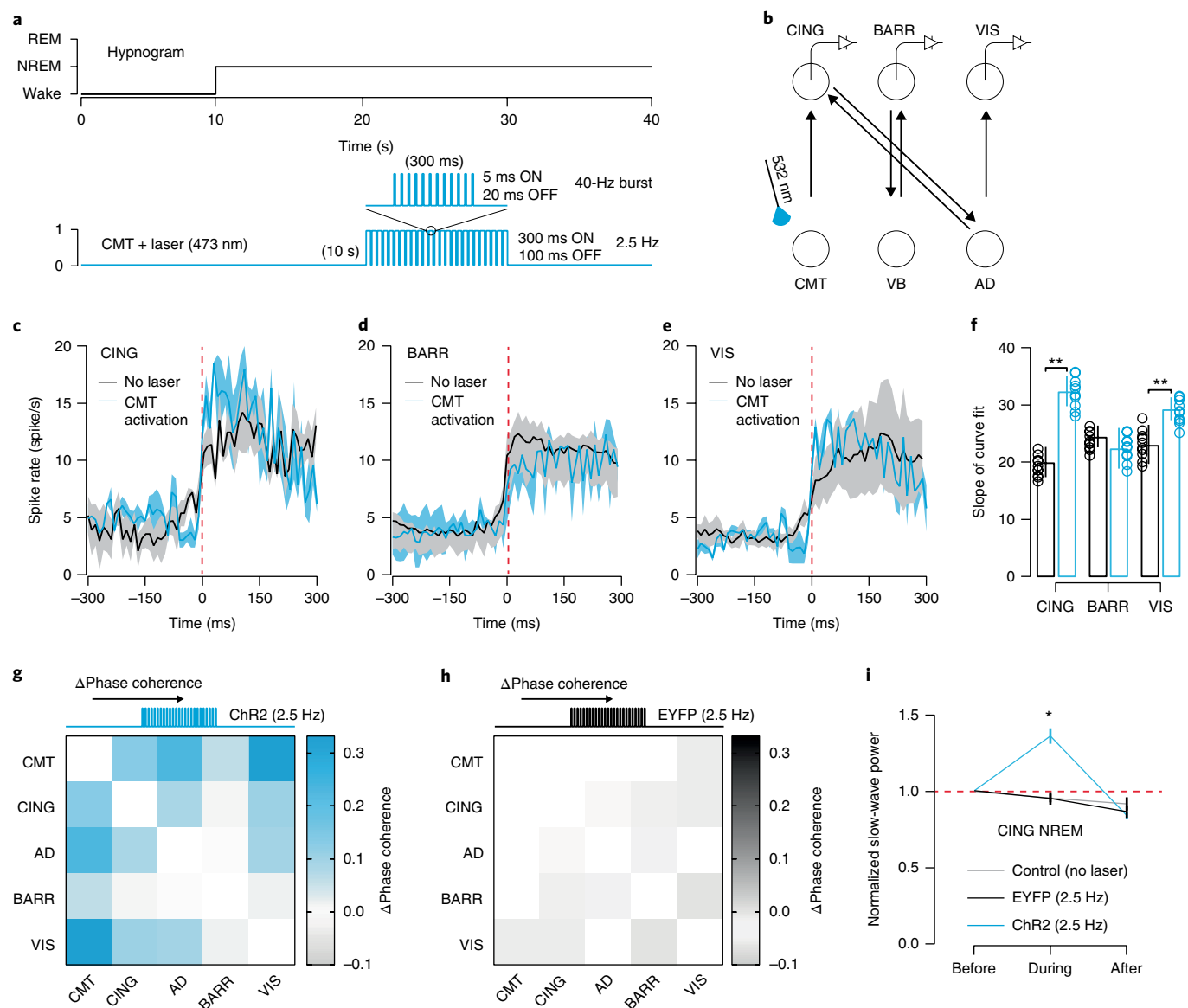


Fig. 6 | CMT neuron firing increases synchrony of cortical UP states. **a**, Experimental timeline showing optogenetic activation of UP-like states (5 ms, 300 ms ON, 100 ms OFF, 10-s duration) in CMT neurons delivered 10 s after the onset of NREM. **b**, Schematic of N-type circuit and instrumentation for chronic implantation of multisite tetrode recordings from CING, BARR, and VIS and optic fiber implants over CMT. AAV2-CaMKII-ChR2-EYFP was stereotactically injected into CMT. **c-e**, Average spiking rates \pm s.e.m. for CING (**c**; $n = 8$ cells), BARR (**d**; $n = 6$ cells), and VIS (**e**; $n = 7$ cells; from $n = 6$ animals) neurons at the onset of the cortical UP states (red dashed line). Spontaneous, black; evoked: blue. **f**, Average slope \pm s.e.m. of curve fits for spiking rates at the start of the cortical UP state (CING: $**P = 0.004$; $t = 3.29$; d.f. = 16; $n = 8$ cells; BARR: $P = 0.62$; $t = 0.51$, d.f. = 12; $n = 6$ cells; VIS: $**P = 0.013$; $t = 2.58$; d.f. = 14; $n = 7$ cells; from $n = 6$ animals; two-sided t test). **g,h**, Averaged change in phase coherence for CMT, CING, AD, BARR, and VIS for blue optical activation of CMT neurons expressing ChR2-EYFP (**g**) and EYFP (**h**). **i**, Averaged delta power \pm s.e.m. in CING 10 s before, during, and 10 s after optogenetic activation of CMT neurons expressing ChR2-EYFP (blue), EYFP (black), and control conditions (gray). Delta power is normalized to the first 10 s of NREM ($*P = 0.0006$; $t = 7.59$; d.f. = 5; $n = 6$ animals; two-sided t test).

one-sided t test; $t = 3.99$; d.f. = 3, from $n = 5$ animals; Fig. 5n). Accordingly, we found that optogenetic silencing of ArchT-EYFP-expressing CING neurons completely prevented the induction of UP-like states in AD and VIS cortical neurons by optogenetic driving of ChR2-EYFP-expressing CMT neurons (Supplementary Fig. 9). Similarly, optogenetic silencing of AD neurons reduced synchrony in VIS neurons ($P = 0.036$; two-sided t test; $t = 6.84$, d.f. = 8; $n = 10$ cells), but not BARR neurons ($P = 0.75$; $n = 9$ cells; from $n = 6$ animals; Fig. 5o-r), and decreased normalized slow-wave power in VIS ($P = 0.011$; $t = 4.63$; d.f. = 4; from $n = 6$ animals; one-sided t test; Fig. 5s). Optogenetic silencing did not induce awakening.

In accordance with the proposed role of the CMT in generating cortical UP states, UP-like states induced by burst-like optogenetic stimulation of CMT neurons (Fig. 6a,b) resulted in increased firing synchrony in CING and VIS across cortical UP states (CING: $P = 0.004$; $t = 3.29$; d.f. = 16; $n = 8$ cells; BARR: $P = 0.62$; $t = 0.51$; d.f. = 12; $n = 6$ cells; VIS: $P = 0.013$; $t = 2.58$; d.f. = 14; two-sided t test; $n = 7$ cells; from $n = 6$ animals; Fig. 6c-f and Supplementary Fig. 9). This was accompanied by an increased phase synchrony between CMT, CING, AD, and VIS in ChR2-EYFP-expressing animals compared to controls (Fig. 6g,h). We further found a significant increase in CING slow-wave power ($P = 0.0006$; $t = 7.59$; d.f. = 5; two-sided t test; $n = 6$ animals; Fig. 6i). Optogenetically evoked

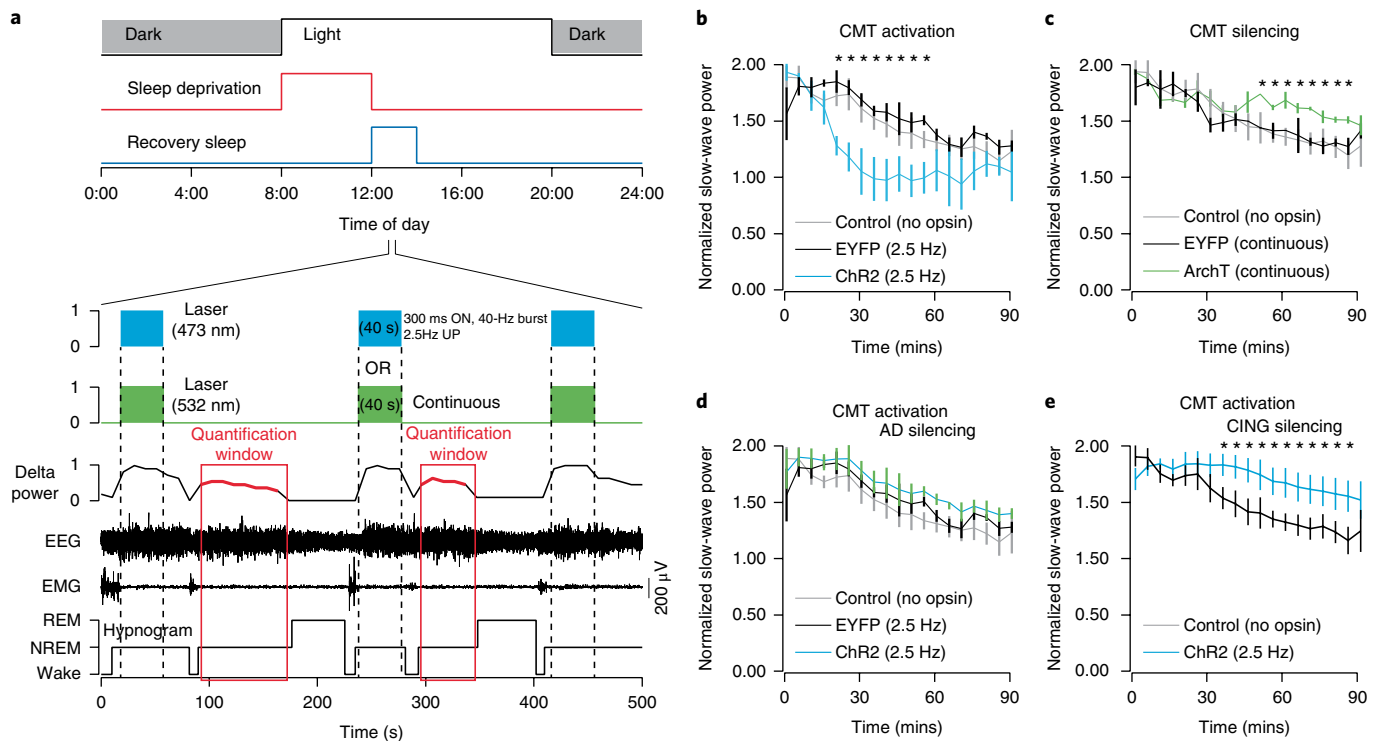


Fig. 7 | CMT neuron activity promotes sleep recovery. **a**, Experimental timeline showing sleep deprivation and sleep recovery protocols. ChR2-EYFP-expressing CMT neurons were activated with blue light (300 ms ON, 100 ms OFF, 40-s duration) and ArchT-EYFP-expressing CMT silenced with green light (40 s of continuous stimulation) during every second NREM period during recovery sleep. The rebound delta power was measured from the interleaving NREM periods. **b–e**, Average delta power \pm s.e.m. during sleep recovery in CING during (**b**) optogenetic stimulation of UP states in CMT neurons ($*P < 0.035$; $t = 4.59$; d.f. = 7; one-way ANOVA; $n = 6$ animals), (**c**) optogenetic silencing of CMT neurons ($*P < 0.027$; $t = 3.86$; d.f. = 5; one-way ANOVA; $n = 6$ animals), (**d**) optogenetic stimulation of CMT neurons with concurrent optogenetic silencing of AD neurons ($P = 0.25$; $t = 1.74$; d.f. = 5; one-way ANOVA; $n = 6$ animals), and (**e**) optogenetic silencing of CING neurons ($*P = 0.013$; $t = 5.68$; d.f. = 4; one-way ANOVA; $n = 5$ animals).

UP-like states during NREM did not induce awakening. These results suggest that CMT neurons contribute to the initiation of UP states in CING, which propagate to VIS via AD relay cells. Note that this does not take account of isolated cortical slow waves originating in parietal or occipital cortices^{18,19}.

CMT neuron activity promotes sleep recovery. During sleep recovery following a period of sleep deprivation, slow-wave power and cortical synchrony are increased^{18,35}, a measure of sleep pressure. In this context, traveling of slow waves has been suggested to promote sleep¹⁹, but direct involvement of mediadorsal thalamocortical networks in sleep recovery has yet to be investigated. We therefore investigated the thalamic contribution to sleep recovery. We measured LFPs and spiking activity during sleep recovery following 4-h sleep deprivation in freely moving mice (Fig. 7a and see Methods). During spontaneous recovery sleep, we found that slow-wave power (normalized to power during baseline sleep) was significantly increased in the CMT (2.0 ± 0.3 ; $P < 0.05$; $t = 3.7$; d.f. = 4), CING (2.7 ± 0.4 ; $P > 0.05$; $t = 4.1$; d.f. = 4), AD (2.7 ± 0.5 ; $P < 0.05$; $t = 3.5$; d.f. = 4), and VIS (2.3 ± 0.3 ; $P < 0.05$; $t = 3.9$; d.f. = 4), but it was not significantly increased in BARR (1.0 ± 0.1 ; $P < 0.05$; $t = 0.6$; d.f. = 4; $n = 6$ animals; one-sided t test; Supplementary Fig. 11 and see below and Discussion). Consistent with this finding, we found a significantly increased synchrony of neuron spiking, revealed by the slope of their curve fits at the onset of the cortical UP state¹⁸, within CMT ($P < 0.05$; $t = 4.12$; d.f. = 12), CING ($P < 0.05$; $t = 4.36$; d.f. = 14), AD ($P < 0.05$; $t = 4.78$; d.f. = 14), and VIS ($P < 0.05$; $t = 4.53$; d.f. = 14; one-sided t test) during sleep recovery, but reduced for neurons in BARR ($P < 0.05$; $t = 4.11$; d.f. = 14; Supplementary Table 1 and Supplementary Figs. 11 and 12). Notably, CMT neurons conserved their phase advancement over

recorded cortical, midline, and sensory thalamic neurons during sleep recovery (Supplementary Figs. 11 and 12). Note that VB, but not CMT, LFPs recordings displayed sleep-like activity—i.e., large-amplitude, low-frequency oscillations—when animals were awake during the sleep deprivation procedure, as evidenced by the increased slow-wave power (Supplementary Fig. 12f,g).

To test whether perturbation of midline thalamus activity alters sleep recovery, we induced cortical slow-wave-like activity by burst-like optogenetic activation of CMT neurons and measured the subsequent slow-wave power in CING during the sleep recovery following 4-h sleep deprivation (Fig. 7a). To exclude direct optogenetic network effects, quantification was conducted on NREM episodes in which no optical stimulation was delivered (Fig. 7a and see Methods). We found that inducing slow-wave-like activity by optogenetic activation of ChR2-EYFP-expressing CMT neurons hastened the sleep recovery process, as measured by a faster reduction in slow-wave power and return to baseline levels ($P < 0.035$; $t = 4.59$; d.f. = 7; one-way ANOVA; $n = 6$ animals; Fig. 7b). In contrast, optogenetic silencing of ArchT-EYFP-expressing CMT neurons retarded the process ($P < 0.027$; $t = 3.86$; d.f. = 5; one-way ANOVA; $n = 6$ animals; Fig. 7c). Simultaneous optogenetic activation and silencing of CMT and AD neurons, respectively, resulted in no change from control animals (i.e., no stimulation; $P = 0.25$; $t = 1.74$; d.f. = 5; one-way ANOVA; $n = 6$ animals; Fig. 7d). Finally, optogenetic silencing of CING neurons similarly delayed the sleep recovery process ($P = 0.013$; $t = 5.68$; d.f. = 4; one-way ANOVA; $n = 5$ animals; Fig. 7e). These results indicate that the sleep recovery process is dependent on synchronized activity throughout the CMT–CING–AD–VIS circuit and the brain-wide propagation of slow waves.

Discussion

An intact midline thalamus is required for proper brain function during both wakefulness and sleep in rodents³² and humans²⁴. Indeed, CMT damage is associated with disturbances of arousal, cognition, and sleep²³, while electrical stimulation of the midline thalamic nuclei, including the CMT, improves behavioral responsiveness in minimally conscious patients²⁴.

CMT neurons are centrally positioned to contribute to cortical UP and Down states, arousal, and consciousness in the mammalian brain. Both the intrinsic and extrinsic control of CMT neuronal firing remains poorly understood, but pharmacological activation of nicotinic acetylcholine receptors and inhibition of potassium channels in the CMT both cause emergence from anesthesia in rats³². This effect was not observed with activation of other midline thalamic nuclei. Together with our results, this suggests that the CMT is a strong modulator of cortical arousal, although whether other midline thalamic nuclei can cause cortical activation remains to be investigated. CMT neurons receive inputs from adrenergic, serotonergic²⁵, GABAergic²⁷, and cholinergic³⁶ neurons. Unlike dorsal and sensory thalamic neurones³⁷, they are more susceptible to depolarization by external inputs originating from subcortical areas, since they do not possess the hyperpolarization-activated (I_h) current. Altogether, this suggests that other intrinsic currents leave them susceptible to synaptic inputs³⁸. In turn, neurons from the midline thalamus, and the CMT in particular, have extensive projections to the frontal cortex and striatum²⁹.

Here we demonstrate a dual-control function of excitatory CMT neurons over sleep slow waves and awakening from NREM sleep, depending on the firing pattern and duration of firing of CMT neurons. Optogenetic tonic activation of CMT neurons reliably induced rapid awakening from NREM when the duration of the optical stimulations was longer than 500 ms, while stimulation mimicking spontaneous burst firing triggered slow-wave-like activity and enhanced cortical synchrony but not awakening. During NREM, CMT neurons contribute to the initiation of cortical UP states in the CING that are synchronized over brain-wide cortical circuits by thalamic AD relay cells; however, despite the accurate anatomical location of our recording sites, genetic targeting of opsin expression extended beyond the anatomical boundaries of CMT and AD (i.e., rhomboides, intermediodorsal nucleus, and laterodorsal thalamus, respectively), and therefore we cannot rule out some contribution of these structures in brain-wide synchronization. Our circuit supports the onset and synchrony of frontal cortical slow waves, but some isolated slow waves may also travel from posterior areas⁹ and propagate via corticocortical pathways¹⁹. These findings suggest that CMT and AD neurons precisely synchronize local¹⁷ and global¹⁰ cortical circuits and may therefore support cognitive processes during NREM sleep, such as slow-wave-dependent memory consolidation³⁹. Indeed, neurodegeneration and low functional MRI activity in AD are associated with high-frequency electroencephalogram oscillations, less cortical synchronization, and reduced amplitude of sleep slow waves⁴⁰ in patients with schizophrenia⁴¹ and Alzheimer's disease⁴². Thus, hypoactivity of AD neurons impairs both the quality and quantity of sleep and may support learning and memory consolidation during sleep via anteroposterior large-scale integration of information during consciousness^{43,44}.

We propose that these frontally generated cortical UP states propagate along an 'N-type' CMT–CING–AD–VIS (i.e., thalamo-cortico-thalamo-cortical) excitatory pathway that is distinct from classical thalamocortical loops in primary somatosensory feedback circuits (for example, VB–BARR cortex loop)^{1,16}. This pathway is important for long-range cortical synchrony of frontally generated slow waves during NREM, sleep recovery, and awakening from NREM through a polysynaptic feedforward pathway that is likely to involve local feedback circuits.

At the cortical level, our results are consistent with the frontal origin of cortical slow waves and their anteroposterior propagation in

the mammalian brain¹⁹, as well as the minimal perturbations of cortical lesions on long-range neocortical connectivity³³ and the confinement of traveling slow waves to the frontal cortex^{19,20}. Our study provides evidence for an important contribution of the thalamus to the onset of cortical UP states. The neocortex is capable of generating slow waves when thalamic inputs have been abolished^{2,7,45}; however, the frequency of the oscillation is different between in vivo and in vitro preparations⁸, suggesting the importance of extrinsic inputs in the timing of slow-wave generation. Furthermore, one study demonstrated that cortical slow-wave activity is transiently reduced during acute in vivo thalamic lesioning, recovering several days afterwards¹⁴, while other studies demonstrate absence of effect of acute midline and intralaminar thalamus⁴⁶ or chronic lesions⁴⁵ on slow-wave or fast cortical activity, suggesting the existence of extrathalamic mechanisms that can support slow wave integrity, sleep–wake cycles, and overall arousal. Collectively these data, together with the present study, implicate the midline and dorsal thalamus in the timing and synchrony of cortical slow waves in the healthy brain and provide an avenue for the investigation of NREM-dependent cognitive processes such as memory consolidation¹⁷.

During recovery sleep, the amplitude of cortical slow waves is correlated with increased synchrony of pyramidal neuron spiking¹⁸ (but see ref. 47). Our present data further implicate subcortical structures, in particular thalamic circuits, as previously suggested by the increased slow-wave activity upon disinhibition of reticular thalamic neurons in mice²⁷. Consistent with this, the N-type circuit provides a network mechanism for regulating increased cortical neuron spiking synchrony and emphasizes a role for midline and higher-order thalamic neurons in the sleep recovery process. Within the somatosensory VB–BARR loop, the absence of increased slow-wave power during recovery sleep may reflect the sustained slow-wave activity during quiet sleep-deprived wakefulness, which may prevent the accumulation of sleep pressure. This latter observation further supports the distinct anatomical and functional role of midline and sensory thalamus in sleep control.

Notably, neurons from CMT and AD, as well as all cortical neurons recorded, showed highest discharge rates during REM sleep¹⁸. This may be due to strong cholinergic inputs from the laterodorsal tegmental nucleus to the midline thalamus⁴⁸. These inputs, and the restricted projections of the mediodorsal thalamus to insular and retrosplenial cortices and the adjacent claustrum⁴⁹, suggest a role for the mediodorsal thalamus in cortical processing of information during REM or consciousness during sleep, as well as memory consolidation⁵⁰, but this remains to be experimentally investigated.

Collectively, our results further distinguish the anatomical and functional roles of midline and sensory thalamus during NREM sleep and strongly suggest that burst and tonic firing patterns of CMT neuronal firing exerts dual control of sleep slow waves and NREM–wake transitions, respectively. This implicates CMT and AD neurons in brain-wide synchronization of cortical activity, in particular in the control of frontal and global cortical activity respectively, during sleep and sleep recovery.

Methods

Methods, including statements of data availability and any associated accession codes and references, are available at <https://doi.org/10.1038/s41593-018-0164-7>.

Received: 14 September 2017; Accepted: 28 April 2018;

Published online: 11 June 2018

References

1. Steriade, M., Nuñez, A. & Amzica, F. Intracellular analysis of relations between the slow (< 1 Hz) neocortical oscillation and other sleep rhythms of the electroencephalogram. *J. Neurosci.* **13**, 3266–3283 (1993).
2. Steriade, M., Nuñez, A. & Amzica, F. A novel slow (< 1 Hz) oscillation of neocortical neurons in vivo: depolarizing and hyperpolarizing components. *J. Neurosci.* **13**, 3252–3265 (1993).

3. Nir, Y. et al. Selective neuronal lapses precede human cognitive lapses following sleep deprivation. *Nat. Med.* **23**, 1474–1480 (2017).
4. Contreras, D. & Steriade, M. Cellular basis of EEG slow rhythms: a study of dynamic corticothalamic relationships. *J. Neurosci.* **15**, 604–622 (1995).
5. Neske, G. T., Patrick, S. L. & Connors, B. W. Contributions of diverse excitatory and inhibitory neurons to recurrent network activity in cerebral cortex. *J. Neurosci.* **35**, 1089–1105 (2015).
6. Zucca, S. et al. An inhibitory gate for state transition in cortex. *eLife* **6**, e26177 (2017).
7. Timofeev, I., Grenier, F., Bazhenov, M., Sejnowski, T. J. & Steriade, M. Origin of slow cortical oscillations in deafferented cortical slabs. *Cereb. Cortex* **10**, 1185–1199 (2000).
8. Sanchez-Vives, M. V. & McCormick, D. A. Cellular and network mechanisms of rhythmic recurrent activity in neocortex. *Nat. Neurosci.* **3**, 1027–1034 (2000).
9. Vyazovskiy, V. V., Faraguna, U., Cirelli, C. & Tononi, G. Triggering slow waves during NREM sleep in the rat by intracortical electrical stimulation: effects of sleep/wake history and background activity. *J. Neurophysiol.* **101**, 1921–1931 (2009).
10. Lőrincz, M. L. et al. A distinct class of slow (~0.2–2 Hz) intrinsically bursting layer 5 pyramidal neurons determines UP/Down state dynamics in the neocortex. *J. Neurosci.* **35**, 5442–5458 (2015).
11. Steriade, M., Contreras, D., Curró Dossi, R. & Nuñez, A. The slow (< 1 Hz) oscillation in reticular thalamic and thalamocortical neurons: scenario of sleep rhythm generation in interacting thalamic and neocortical networks. *J. Neurosci.* **13**, 3284–3299 (1993).
12. Hughes, S. W., Cope, D. W., Blethyn, K. L. & Crunelli, V. Cellular mechanisms of the slow (< 1 Hz) oscillation in thalamocortical neurons in vitro. *Neuron* **33**, 947–958 (2002).
13. David, F. et al. Essential thalamic contribution to slow waves of natural sleep. *J. Neurosci.* **33**, 19599–19610 (2013).
14. Lemieux, M., Chen, J. Y., Lonjers, P., Bazhenov, M. & Timofeev, I. The impact of cortical deafferentation on the neocortical slow oscillation. *J. Neurosci.* **34**, 5689–5703 (2014).
15. Sherozhiya, M. & Timofeev, I. Global intracellular slow-wave dynamics of the thalamocortical system. *J. Neurosci.* **34**, 8875–8893 (2014).
16. Poulet, J. F., Fernandez, L. M., Crochet, S. & Petersen, C. C. Thalamic control of cortical states. *Nat. Neurosci.* **15**, 370–372 (2012).
17. Huber, R., Ghilardi, M. F., Massimini, M. & Tononi, G. Local sleep and learning. *Nature* **430**, 78–81 (2004).
18. Vyazovskiy, V. V. et al. Cortical firing and sleep homeostasis. *Neuron* **63**, 865–878 (2009).
19. Massimini, M., Huber, R., Ferrarelli, F., Hill, S. & Tononi, G. The sleep slow oscillation as a traveling wave. *J. Neurosci.* **24**, 6862–6870 (2004).
20. Nir, Y. et al. Regional slow waves and spindles in human sleep. *Neuron* **70**, 153–169 (2011).
21. Giber, K. et al. A subcortical inhibitory signal for behavioral arrest in the thalamus. *Nat. Neurosci.* **18**, 562–568 (2015).
22. Liu, J. et al. Frequency-selective control of cortical and subcortical networks by central thalamus. *eLife* **4**, e09215 (2015).
23. Bassetti, C., Mathis, J., Gugger, M., Lovblad, K. O. & Hess, C. W. Hypersomnia following paramedian thalamic stroke: a report of 12 patients. *Ann. Neurol.* **39**, 471–480 (1996).
24. Schiff, N. D. et al. Behavioural improvements with thalamic stimulation after severe traumatic brain injury. *Nature* **448**, 600–603 (2007).
25. Royce, G. J., Bromley, S. & Gracco, C. Subcortical projections to the centromedian and parafascicular thalamic nuclei in the cat. *J. Comp. Neurol.* **306**, 129–155 (1991).
26. Krout, K. E., Belzer, R. E. & Loewy, A. D. Brainstem projections to midline and intralaminar thalamic nuclei of the rat. *J. Comp. Neurol.* **448**, 53–101 (2002).
27. Herrera, C. G. et al. Hypothalamic feedforward inhibition of thalamocortical network controls arousal and consciousness. *Nat. Neurosci.* **19**, 290–298 (2016).
28. McKenna, J. T. & Vertes, R. P. Afferent projections to nucleus reuniens of the thalamus. *J. Comp. Neurol.* **480**, 115–142 (2004).
29. Vertes, R. P., Hoover, W. B. & Rodriguez, J. J. Projections of the central medial nucleus of the thalamus in the rat: node in cortical, striatal and limbic forebrain circuitry. *Neuroscience* **219**, 120–136 (2012).
30. Van der Werf, Y. D., Witter, M. P. & Groenewegen, H. J. The intralaminar and midline nuclei of the thalamus. Anatomical and functional evidence for participation in processes of arousal and awareness. *Brain Res. Brain Res. Rev.* **39**, 107–140 (2002).
31. Baker, R. et al. Altered activity in the central medial thalamus precedes changes in the neocortex during transitions into both sleep and propofol anaesthesia. *J. Neurosci.* **34**, 13326–13335 (2014).
32. Lioudyno, M. I. et al. Shaker-related potassium channels in the central medial nucleus of the thalamus are important molecular targets for arousal suppression by volatile general anesthetics. *J. Neurosci.* **33**, 16310–16322 (2013).
33. Contreras, D., Destexhe, A., Sejnowski, T. J. & Steriade, M. Control of spatiotemporal coherence of a thalamic oscillation by corticothalamic feedback. *Science* **274**, 771–774 (1996).
34. Van Groen, T. & Wyss, J. M. Projections from the anterodorsal and anteroventral nucleus of the thalamus to the limbic cortex in the rat. *J. Comp. Neurol.* **358**, 584–604 (1995).
35. Borbély, A. A. A two process model of sleep regulation. *Hum. Neurobiol.* **1**, 195–204 (1982).
36. Alkire, M. T., McReynolds, J. R., Hahn, E. L. & Trivedi, A. N. Thalamic microinjection of nicotine reverses sevoflurane-induced loss of righting reflex in the rat. *Anesthesiology* **107**, 264–272 (2007).
37. McCormick, D. A. & Pape, H. C. Properties of a hyperpolarization-activated cation current and its role in rhythmic oscillation in thalamic relay neurones. *J. Physiol. (Lond.)* **431**, 291–318 (1990).
38. Jhangiani-Jashanmal, I. T., Yamamoto, R., Gungor, N. Z. & Paré, D. Electroresponsive properties of rat central medial thalamic neurons. *J. Neurophysiol.* **115**, 1533–1541 (2016).
39. Mölle, M., Bergmann, T. O., Marshall, L. & Born, J. Fast and slow spindles during the sleep slow oscillation: disparate coexistence and engagement in memory processing. *Sleep* **34**, 1411–1421 (2011).
40. Wulff, K., Gatti, S., Wettstein, J. G. & Foster, R. G. Sleep and circadian rhythm disruption in psychiatric and neurodegenerative disease. *Nat. Rev. Neurosci.* **11**, 589–599 (2010).
41. Uhlhaas, P. J. & Singer, W. Abnormal neural oscillations and synchrony in schizophrenia. *Nat. Rev. Neurosci.* **11**, 100–113 (2010).
42. Zarei, M. et al. Combining shape and connectivity analysis: an MRI study of thalamic degeneration in Alzheimer's disease. *Neuroimage* **49**, 1–8 (2010).
43. Kinomura, S., Larsson, J., Gulyás, B. & Roland, P. E. Activation by attention of the human reticular formation and thalamic intralaminar nuclei. *Science* **271**, 512–515 (1996).
44. Schmitt, L. I. et al. Thalamic amplification of cortical connectivity sustains attentional control. *Nature* **545**, 219–223 (2017).
45. Fuller, P. M., Sherman, D., Pedersen, N. P., Saper, C. B. & Lu, J. Reassessment of the structural basis of the ascending arousal system. *J. Comp. Neurol.* **519**, 933–956 (2011).
46. Anaclet, C. et al. Basal forebrain control of wakefulness and cortical rhythms. *Nat. Commun.* **6**, 8744 (2015).
47. Rodriguez, A. V. et al. Why does sleep slow-wave activity increase after extended wake? Assessing the effects of increased cortical firing during wake and sleep. *J. Neurosci.* **36**, 12436–12447 (2016).
48. Steriade, M., Datta, S., Paré, D., Oakson, G. & Curró Dossi, R. C. Neuronal activities in brain-stem cholinergic nuclei related to tonic activation processes in thalamocortical systems. *J. Neurosci.* **10**, 2541–2559 (1990).
49. Shibata, H. & Honda, Y. Thalamocortical projections of the anterodorsal thalamic nucleus in the rabbit. *J. Comp. Neurol.* **520**, 2647–2656 (2012).
50. Boyce, R., Glasgow, S. D., Williams, S. & Adamantidis, A. Causal evidence for the role of REM sleep theta rhythm in contextual memory consolidation. *Science* **352**, 812–816 (2016).

Acknowledgements

We thank the Tidis laboratory members for their technical help and comments on a previous version of the manuscript. We thank M. Mamelì, S. Brown, and C. Bassetti for helpful comments on the manuscript. We thank the laboratory of H.-R. Widmer and the M.I.C. UNIBE Facility for the use of the microscopes. Optogenetic plasmids were kindly provided by K. Deisseroth (Stanford University) and E. Boyden (MIT). A.R.A. was supported by the Human Frontiers Science Program (RGY0076/2012), Inselspital University Hospital, the University of Bern, Swiss National Science Foundation (156156), and the European Research Council (ERC-2016-COG-725850).

Author contributions

T.C.G. and A.R.A. conceived the study. T.C.G. and C.G.H. collected the data. T.C.G. and M.B. analyzed the data. A.R.A. supervised the project. All authors wrote the manuscript.

Competing interests

The authors declare no competing interests.

Additional information

Supplementary information is available for this paper at <https://doi.org/10.1038/s41593-018-0164-7>.

Reprints and permissions information is available at www.nature.com/reprints.

Correspondence and requests for materials should be addressed to A.R.A.

Publisher's note: Springer Nature remains neutral with regard to jurisdictional claims in published maps and institutional affiliations.

Methods

Animals. We used C57Bl6 adult male mice (6–14 weeks old) from Charles Rivers Laboratories, Germany. Animals were housed in individual, custom-designed polycarbonate cages at constant temperature ($22 \pm 1^\circ\text{C}$), humidity (30–40%), and circadian cycle (12-h light–dark cycle, lights on at 08:00). Food and water were available ad libitum. Animals were treated according to protocols and guidelines approved by the Veterinary Office of the Canton of Bern, Switzerland (license number BE 113/13). Animals were housed in IVC cages in groups of 2–5 before instrumentation and after virus injections. After implantation, all mice were housed individually. Animals were habituated to the recording cable and optical fibers in their open-top home cages (300 × 170 mm) and kept tethered for the duration of the experiments. Animals were allowed to move freely in the cage during *in vivo* electrophysiology experiments. Before commencing experimental recording, baseline sleep was recorded and compared to previously published results⁵¹ to confirm resumption of a normal sleep–wake cycle after instrumentation. Experiments were performed during the ‘lights-on’ period (12:00–16:00). Viral injections were performed at 6–8 weeks of age and instrumentation at 10–12 weeks of age. All recordings were performed from 11–14 weeks of age. No animals were excluded from analysis.

Stereotaxic injection of AAV. Six-week-old C57Bl6 mice were anaesthetized in isoflurane (4.0% for induction, 1.0–1.5% for maintenance) in oxygen and mounted in a stereotaxic frame (Model 940, David Kopf Instruments). Saline (10 mL/kg) and meloxicam (5 mg/kg) were given subcutaneously before incision. The skin on the head was shaved and aseptically prepared, and 2 mg/kg lidocaine infused subcutaneously at the incision site. A single longitudinal midline incision was made from the level of the lateral canthus of the eyes to the lambda skull suture. Injections were performed using a 28-gauge needle (Plastics One) connected by mineral oil-filled tubing to a 10- μL Hamilton syringe in an infusion pump (Model 1200, Harvard Apparatus). Injections were performed at 0.1 $\mu\text{L}/\text{min}$ and the needle left *in situ* for 10 min afterwards to allow diffusion. Injections were performed in CMT (AP -1.7 mm, ML $+1.0$ mm, DV -3.8 mm, 15° , 100 nL), AD (AP -0.9 mm, ML ± 0.8 mm, DV -3.2 mm, 150 nL), and CING (AP $+1.8$ mm, ML $+0.2$ mm, DV -1.6 mm, 100 nL). Coordinates based on the mouse brain atlas⁵². Animals were randomly assigned to receive either AAV2-CaMKII-E1fa-ChR2-EYFP for optical stimulation or AAV2-CaMKII-E1fa-EYFP as control for direct retinal stimulation of CMT and VB. For experiments in Fig. 3c,d, animals were randomly assigned to receive injections in either CMT or VB. Silencing of AD or CING was achieved with AAV2-CaMKII-E1fa-ArchT3.0-EYFP, and AAV2-CaMKII-E1fa-ChR2-mCherry was used for anatomical tracing of projections from the CING. All plasmids were obtained from University of North Carolina Vector Core Facility. Animals were allowed to recover for 3 weeks before instrumentation or being killed for histology.

Instrumentation. Animals were anaesthetized by isoflurane in oxygen and mounted in a stereotaxic frame. Saline (10 mL/kg) and meloxicam (5 mg/kg) were given subcutaneously. The skin on the head was shaved and aseptically prepared, and 2 mg/kg lidocaine infused subcutaneously at the incision site. A single longitudinal midline incision was made from the level of the lateral canthus of the eyes to the lambda skull suture. Three stainless steel screws were placed in the skull to measure EEG (EEG: AP -2.3 mm, ML ± 2.0 mm; REF: AP -4.3 mm, ML $+0.5$ mm) and two bare-ended wires sutured to the trapezius muscle of the neck to record EMG. Tetrodes were made from four strands of 10- μm twisted tungsten wire (CFW0010954, California Fine Wire) connected to an electrode interface board by gold pins and were inserted into the CMT (AP -1.7 mm, ML $+1.0$ mm, DV -3.8 mm, 15°), CING (AP $+1.8$ mm, ML $+0.2$ mm, DV -1.6 mm), AD (AP -0.9 mm, ML ± 0.8 mm, DV -3.2 mm), BARR (AP -2.0 mm, ML $+2.2$ mm, DV -1.1 mm), and VIS (AP -3.3 mm, ML $+2.5$ mm, DV -0.9 mm) and secured to the skull with dental acrylic (C&B Metabond). Linear array electrodes (A1x16-5mm-100-177-CM16LP, Neuronexus) were implanted (AP -1.7 mm, ML ± 0.0 mm, DV -4.0 mm) to record from all midline thalamic nuclei ($n = 6$ animals). Optic fibers of 200- μm diameter were placed in the CMT (AP -1.7 mm, ML $+1.0$ mm, DV -3.8 mm, 15°), bilaterally in VB (AP -1.7 mm, ML ± 1.8 mm, DV -3.3 mm), and bilaterally in AD (AP -0.9 mm, ML ± 0.8 mm, DV -3.0 mm) and secured with the same dental acrylic. Optical stimulation of CMT axon terminals was performed with bilateral fibers in CING (AP $+1.8$ mm, ML ± 0.2 mm, DV -1.3 mm), ZI (AP -0.9 mm, ML ± 0.5 mm, DV -4.3 mm), and insular cortex (AP $+0.5$ mm, ML ± 2.3 mm, DV -4.9 mm, 20°). For experiments in Fig. 3h, animals were randomly assigned to have optic fibers implanted in CING, ZI, or insular cortex. Finally, the implant was stabilized using methyl methacrylate cement and the animal was allowed to recover in its home cage on top of a heating mat. Animals were allowed a minimum of 5 d to recover before starting recordings.

Data acquisition. For experiments presented in Fig. 3, mice were connected to a multichannel cable. EEG/EMG data was amplified ($\times 1,000$) by an analog amplifier (Model 3500, AM Systems) and digitized at 200 Hz via a digital–analog converter (NIDAQ 6363, National Instruments). For all other recordings, mice were connected to a tethered digitizing headstage (RHD2132, Intan Technologies) and data sampled at 20 kHz recorded in free open-source software (RHD2000

evaluation software, Intan Technologies). Optical fibers were connected to a patch chord using a zirconia sleeve (Doric Lenses). The patch chords were coated in black furcation tubing and connections covered in black varnish to prevent ocular stimulation from the laser. Habituation to the cables was performed up to 8 h per day until the animals had nested and resumed a normal sleep–wake cycle. To ensure that a correct sleep–wake cycle had been regained following instrumentation, we recorded a baseline of natural sleep from ZT 4 to 9 and compared the results to previously published works (Supplementary Fig. 1 and ref.²⁷). All optogenetic experiments were performed between ZT 4 and 8. Optogenetic stimulation was performed with blue light (473 nm) from a laser (LRS-0473-PFM-00100-05, Laserglow Technologies) via a patch chord, 10 s after the start of NREM, judged by an experienced experimenter in real time, as an appropriate latency to consider ongoing NREM sleep episodes as stable as described previously^{27,53}. Optical inhibition was performed with green light (532 nm) from a laser (LRS-0532-GFM-00100-03, Laserglow Technologies), also via a patch chord. Laser output was controlled using TTL from a pulse generator (Master-9, AMPI or PulsePal 2, Sanworks). TTL signals were co-acquired with all recordings.

Awakening was assessed by an abrupt increase in EMG activation, often accompanied with movements, concurrent with cortical activation, typically assessed by increased frequency and decreased amplitude of the EEG, as previously reported by us^{27,53} and others⁵⁴.

Signal processing. Sleep scoring was performed manually, based on frequency and amplitude characteristics of the EEG and EMG in custom software written in Matlab and using 1-s epochs to allow accurate tracking of microarousals^{55,56}. We defined NREM as high-amplitude, synchronous activity in the EEG with a delta (1- to 4.5-Hz) frequency dominating the signal and low EMG amplitude, defined REM as highly synchronous theta (5- to 10-Hz) and flat EMG, and defined wake as increased EMG activity. The start of wake was defined as the first epoch with a rapid increase in muscle tone concurrent with a low-amplitude, high-frequency (>6 Hz) EEG, NREM was defined as the epoch containing the first slow wave of more than 200- μV amplitude, wake was defined as the first epoch with a rapid increase in muscle tone, and REM was defined as the first epoch with a reduced EMG tone and consolidated theta:delta ratio more than 1. In cases where EEG/EMG was co-acquired with unit activity, data was downsampled to 500 Hz before scoring sleep stages by applying a low-pass filter (200 Hz, Chebyshev Type I, order 8, 0.05-dB passband ripple) to prevent aliasing. During scoring, the experimenter was blinded to the timing of any optogenetic manipulation but not to the conditions of the experiment.

Multitunit activity was first extracted from bandpass-filtered recordings (600- to 4,000-Hz, fourth-order elliptic filter, 0.1-dB passband ripple, -40 dB stopband attenuation). Filtering was performed in both the forward and reverse directions. The detection threshold was set as $7.5\times$ the median of the absolute value of the filtered signal. The detected multitunit activity was then sorted using the WaveClus toolbox⁵⁷ to obtain single units. Briefly, a four-level Haar discrete wavelet transform (wavedec, Matlab) was applied to the detected multitunit activity, and the ten most-discriminative wavelet coefficients were selected using the Kolmogorov–Smirnov test. Selected wavelet coefficients were subsequently sorted using the super-paramagnetic clustering, as described previously⁵⁷, to obtain single units. Sorted spikes were visually inspected and clusters with a completely symmetric shape or an average firing rate less than 0.2 Hz were discarded from the analyses. Stage-specific interspike interval (ISI) histograms were created for individual units using a 1-ms bin width. For cortical recordings, neurons with average firing rates >20 spikes/s were omitted from the analysis as they were likely to be interneurons. Interneurons were excluded from analysis, as VIP⁺ cells do not participate in cortical slow wave generation⁵⁸ and could not be differentiated from SOM⁺ interneurons in our preparation.

Burst firing of single units was detected as a minimum of three consecutive action potentials with ISI < 6 ms and preceded by a quiescent hyperpolarized state of at least 50 ms⁵⁸. The interburst interval (IBI) was defined as the distance between the centers of two consecutive bursting activities during NREM episodes. IBI histograms during NREM sleep were created for individual units using a 200-ms bin width.

To detect UP/Down states, LFP/EEG signals were first bandpass-filtered (at 0.5–3 Hz) using window-based finite impulse response filter (fir1, Matlab), with an order equal to three cycles of low cutoff frequency, in forward and reverse directions to provide zero-phase distortion (filtfilt, Matlab). Individual UP–Down states were detected from zero-crossing of filtered signals. The onset of UP states was defined as zero-crossing from negative to positive. To secure our analysis, we excluded individual UP–Down states that were shorter than 200 ms or had absolute amplitude < 1 s.d. from the mean.

For each unit, the average firing rate during vigilance state was calculated as the total number of action potentials during a state divided by total time spent in that state and reported in Hz. Mean firing rates during vigilance state transition were calculated by averaging firing rates across transitions using a non-overlapping moving window of 100 ms. Mean firing rates during transition from Down to UP states were calculated by averaging firing rates of all detected Down to UP transitions using a non-overlapping moving window of 10 ms. Mean firing rates

were then fitted with a Boltzmann sigmoidal curve in GraphPad Prism using the following equation:

$$y = \text{minimum} + \frac{\text{maximum} - \text{minimum}}{1 + \frac{t_{1/2} - x}{\text{slope}}}$$

Where y is the neuronal firing rate and x is time. The half-times of the curves ($t_{1/2}$) were used for comparison of lag and phase. The slopes of the curve fits at the half-time point were used as a measure of neuronal firing modulation and therefore synchrony¹⁸.

Power spectral density (PSD) was estimated using Welch's method (pwlch, Matlab), using 8-s windows having 75% overlap, with 0.5-Hz resolution. Delta power in a recording segment was calculated using a modified periodogram (bandpower, Matlab), considering the estimated Welch's PSD in 0.5–4 Hz. Delta power during optogenetic perturbations was estimated for 10-s recording segments before, during, and after perturbation. NREM delta power during recovery sleep was calculated using a moving window of 10 min having 50% overlap and was normalized to the power in the same frequency bin during baseline sleep (i.e., no sleep deprivation) for each animal. This normalization corrects for variations in recorded signals across animals, which are mainly the result of different electrode impedances.

Phase synchronization between each pair of thalamic and cortical LFP recordings during spontaneous and optogenetic perturbations of NREM sleep were estimated using mean phase coherence³⁹. To measure delta phase coherence, LFP signals were first filtered in the delta range (0.5–4 Hz) using a 6,000th-order FIR filter (fir1, Matlab) in both the forward and reverse directions. Afterward, the instantaneous phases of delta oscillations were estimated using the Hilbert transform. Delta-phase coherence was obtained by averaging the instantaneous phase differences of two filtered signals projected onto a unit circle in the complex plane. The estimated measure falls within a [0, 1] interval, where zero and one indicate completely incoherent and coherent delta rhythms, respectively.

To average the data acquired from linear array electrodes, we normalized the recording spots across animals on the basis of histological findings. Changes in spike timing were averaged across reference points (behavioral transitions or detected UP states) and fitted with a Boltzmann sigmoidal curve (see equation above). The slopes and relative half-times of these curves were then extrapolated.

Synchrony was determined by the slope of neuron firing or LFPs at the onset of cortical UP state, as previously described⁶⁰.

Sleep deprivation. Animals were moved from the home cage to a new cage with clean bedding, food and water, and a novel red plastic object at 08:00 (ZT 0). Gentle handling was performed when animals were stationary to prevent sleep. Four hours later (ZT 4) they were returned to their original home cage and EEG/EMG and spike/LFP recordings were obtained between ZT 4 and 9.

Immunohistochemistry. Animals were deeply anaesthetized with 15 mg pentobarbital (i.p.) and the heart transfused with 20 ml ice-cold, heparinized PBS, followed by 30 mL 4% formalin. Brains were removed and postfixed overnight in 4% formalin. They were then cryoprotected in 40% sucrose for 24–48 h. Sections 30 μ m thick were cut in a cryostat. Free-floating sections were washed in PBS + 0.1% Triton X-100 (PBS-T) three times for 10 min each and then blocked by incubation with 4% bovine serum albumin in PBS-T for 1 h. Free-floating sections were incubated with primary antibodies for GFP (Life Technologies: A10262; 1:4,000) for 24–48 h at 4 °C. They were then washed in PBS-T three times for 10 min each and then incubated with the secondary antibody (Abcam: AB96947, 1:500) for 1 h at room temperature (20–22 °C).

Confirmation of electrode placement was performed in brain sections stained with bisbenzimidazole as a counter stain to the DIO that coated the electrodes. Briefly, free-floating brain slices were exposed to bisbenzimidazole (1 μ g/mL) in PBS for 15 min at room temperature. Three washes of 15 min each in PBS were then performed, and slices were then mounted on glass slides and allowed to dry. A cover slip was placed on the slices, with a mounting medium, and they were then imaged on a confocal fluorescent microscope.

Statistical analysis. Matlab (MathWorks) and Prism 6 (GraphPad) were used for statistical analysis. No power calculations were performed to determine sample sizes, but similarly sized cohorts were used in other relevant investigations²⁷. Data were compared via one-way ANOVA, or t tests for parametric data, with post hoc Tukey's corrections for multiple comparisons. Data distribution was assumed to be normal, but this was not formally tested. Values in the text are reported as mean \pm standard error mean (s.e.m.) unless reported otherwise. Figs. were prepared in Adobe CS6 (Adobe).

Reporting Summary. Further information on experimental design is available in the Life Sciences Reporting Summary linked to this article.

Data and code availability. The data that support the findings of this study and the Matlab code used for analysis are available from the corresponding author upon reasonable request.

References

- Jego, S. et al. Optogenetic identification of a rapid eye movement sleep modulatory circuit in the hypothalamus. *Nat. Neurosci.* **16**, 1637–1643 (2013).
- Paxinos, G. & Franklin, K. B. J. *The Mouse Brain in Stereotaxic Coordinates*. 4th edn. (Academic Press, Cambridge, MA, 2012).
- Adamantidis, A. R., Zhang, F., Aravanis, A. M., Deisseroth, K. & de Lecea, L. Neural substrates of awakening probed with optogenetic control of hypocretin neurons. *Nature* **450**, 420–424 (2007).
- Kroeger, D. et al. Cholinergic, glutamatergic, and GABAergic neurons of the pedunculopontine tegmental nucleus have distinct effects on sleep/wake behavior in mice. *J. Neurosci.* **37**, 1352–1366 (2017).
- McShane, B. B. et al. Characterization of the bout durations of sleep and wakefulness. *J. Neurosci. Methods* **193**, 321–333 (2010).
- Morairty, S. R. et al. A role for cortical nNOS/NK1 neurons in coupling homeostatic sleep drive to EEG slow wave activity. *Proc. Natl Acad. Sci. USA* **110**, 20272–20277 (2013).
- Quiroga, R. Q., Nadasdy, Z. & Ben-Shaul, Y. Unsupervised spike detection and sorting with wavelets and superparamagnetic clustering. *Neural Comput.* **16**, 1661–1687 (2004).
- Guido, W., Lu, S. M. & Sherman, S. M. Relative contributions of burst and tonic responses to the receptive field properties of lateral geniculate neurons in the cat. *J. Neurophysiol.* **68**, 2199–2211 (1992).
- Mormann, F., Lehnertz, K., David, P. & Elger, E. C. Mean phase coherence as a measure for phase synchronization and its application to the EEG of epilepsy patients. *Physica. D* **144**, 358–369 (2000).
- Fattinger, S., Jenni, O. G., Schmitt, B., Achermann, P. & Huber, R. Overnight changes in the slope of sleep slow waves during infancy. *Sleep* **37**, 245–253 (2014).

Reporting Summary

Nature Research wishes to improve the reproducibility of the work that we publish. This form provides structure for consistency and transparency in reporting. For further information on Nature Research policies, see [Authors & Referees](#) and the [Editorial Policy Checklist](#).

Statistical parameters

When statistical analyses are reported, confirm that the following items are present in the relevant location (e.g. figure legend, table legend, main text, or Methods section).

n/a Confirmed

- The exact sample size (n) for each experimental group/condition, given as a discrete number and unit of measurement
- An indication of whether measurements were taken from distinct samples or whether the same sample was measured repeatedly
- The statistical test(s) used AND whether they are one- or two-sided
Only common tests should be described solely by name; describe more complex techniques in the Methods section.
- A description of all covariates tested
- A description of any assumptions or corrections, such as tests of normality and adjustment for multiple comparisons
- A full description of the statistics including central tendency (e.g. means) or other basic estimates (e.g. regression coefficient) AND variation (e.g. standard deviation) or associated estimates of uncertainty (e.g. confidence intervals)
- For null hypothesis testing, the test statistic (e.g. F , t , r) with confidence intervals, effect sizes, degrees of freedom and P value noted
Give P values as exact values whenever suitable.
- For Bayesian analysis, information on the choice of priors and Markov chain Monte Carlo settings
- For hierarchical and complex designs, identification of the appropriate level for tests and full reporting of outcomes
- Estimates of effect sizes (e.g. Cohen's d , Pearson's r), indicating how they were calculated
- Clearly defined error bars
State explicitly what error bars represent (e.g. SD, SE, CI)

Our web collection on [statistics for biologists](#) may be useful.

Software and code

Policy information about [availability of computer code](#)

Data collection

Matlab 2015b and Intan RHD2000 (1.5.2) were used for the collection of data in this study.

Data analysis

Signal processing was performed using custom written algorithms in Mathworks Matlab (v. 2015b). Cell spiking activity was detected and sorted using the WaveClus toolbox in Matlab. Algorithms are not published, but will be made available to authors and reviewers on request. Fluorescence intensity was measured in ImageJ. Statistical analysis was performed using preset algorithms in Graphpad Prism (v. 6). Figures were prepared in Adobe Illustrator CS6.

For manuscripts utilizing custom algorithms or software that are central to the research but not yet described in published literature, software must be made available to editors/reviewers upon request. We strongly encourage code deposition in a community repository (e.g. GitHub). See the Nature Research [guidelines for submitting code & software](#) for further information.

Data

Policy information about [availability of data](#)

All manuscripts must include a [data availability statement](#). This statement should provide the following information, where applicable:

- Accession codes, unique identifiers, or web links for publicly available datasets
- A list of figures that have associated raw data
- A description of any restrictions on data availability

All data and analysis code are available on request from the corresponding author.

Field-specific reporting

Please select the best fit for your research. If you are not sure, read the appropriate sections before making your selection.

Life sciences Behavioural & social sciences Ecological, evolutionary & environmental sciences

For a reference copy of the document with all sections, see [nature.com/authors/policies/ReportingSummary-flat.pdf](https://www.nature.com/authors/policies/ReportingSummary-flat.pdf)

Life sciences study design

All studies must disclose on these points even when the disclosure is negative.

Sample size	No power calculations were performed to determine sample sizes, however similar sized cohorts were used in other relevant investigations (Herrera et al., 2016. Nat. Neuroscience.).
Data exclusions	No animals were excluded from analysis.
Replication	Replication of the neuronal firing and LFPS were dependent on recording independent animals during different recording sessions. Anatomical studies (Supplementary Figs. 3, 6, 7) were replicated in 6 animals for each condition.
Randomization	Animals used for data collection in Fig. 3b, c, d were randomly assigned to receive injections of either AAV2-CamKII-ChR2-EYFP or AAV2-CamKII-EYFP in either VB or CMT. Animals used for data collection in Fig. 3h were randomly assigned for optic fibre implantation in either CING, ZI or insular cortex. Stimulation paradigms were administered in a randomised order. Animals for data collection in Figs. 5 & 6 were randomly assigned to receive injections of either AAV2-CamKII-ChR2-EYFP or AAV2-CamKII-EYFP in CMT.
Blinding	Sleep scoring was performed blinded to the timing of laser stimulations, when present.

Reporting for specific materials, systems and methods

Materials & experimental systems

n/a	Involved in the study
<input checked="" type="checkbox"/>	<input type="checkbox"/> Unique biological materials
<input type="checkbox"/>	<input checked="" type="checkbox"/> Antibodies
<input checked="" type="checkbox"/>	<input type="checkbox"/> Eukaryotic cell lines
<input checked="" type="checkbox"/>	<input type="checkbox"/> Palaeontology
<input type="checkbox"/>	<input checked="" type="checkbox"/> Animals and other organisms
<input checked="" type="checkbox"/>	<input type="checkbox"/> Human research participants

Methods

n/a	Involved in the study
<input checked="" type="checkbox"/>	<input type="checkbox"/> ChIP-seq
<input checked="" type="checkbox"/>	<input type="checkbox"/> Flow cytometry
<input checked="" type="checkbox"/>	<input type="checkbox"/> MRI-based neuroimaging

Antibodies

Antibodies used	The following commercially available antibodies were used: Primary: Chicken IgY-anti GFP (Invitrogen A10262, lot no. 45351A), dilution 1:4000 Secondary: Goat-anti Chicken IgY 488 (Abcam ab96947, lot no. GR263078-11), dilution 1:500
Validation	Concentrations were used based on validation in mice in previous publications (see: Jego et al., 2013 Nat. Neuroscience; Herrera et al., 2016 Nat. Neuroscience).

Animals and other organisms

Policy information about [studies involving animals](#); [ARRIVE guidelines](#) recommended for reporting animal research

Laboratory animals

C57Bl6 male mice, 6 - 13 weeks old, were used.

Wild animals

No wild animals were used in this study.

Field-collected samples

No field samples were collected for analysis in this study.